The SATIN project - I. Turbulent multiphase ISM in Milky Way simulations with SNe feedback from stellar clusters

Bieri, R.; Naab, T.; Geen, S.; Coles, J.P.; Pakmor, R.; Walch, S.

DOI
10.1093/mnras/stad1710

Publication date
2023

Document Version
Final published version

Published in
Monthly Notices of the Royal Astronomical Society

Monthly Notices of the ROYAL ASTRONOMICAL SOCIETY

MNRAS **523,** 6336–6359 (2023) https://doi.org/10.1093/mnras/stad1710
Advance Access publication 2023 June 14

The SATIN project – I. Turbulent multiphase ISM in Milky Way simulations with SNe feedback from stellar clusters

Rebekka Bieri [1★], Thorsten Naab,[2] Sam Geen [3], Jonathan P. Coles [4], Rüdiger Pakmor [2] and Stefanie Walch[5]

[1]*Institute for Computational Science, University of Zurich, Winterthurerstrasse 190, CH-8057 Zürich, Switzerland*
[2]*Max-Planck-Institute for Astrophysics, Karl-Schwartzschild-Strasse 1, D-85748 Garching, Germany*
[3]*Anton Pannekoek Institute for Astronomy, Universiteit van Amsterdam, Science Park 904, NL-1098 XH Amsterdam, the Netherlands*
[4]*ETH Zurich / Swiss National Supercomputing Centre (CSCS), Via Trevano 131, CH-6900 Lugano, Switzerland*
[5]*Physikalisches Institut der Universität zu Köln, Zülpicher Strasse 77, D-50937 Köln, Germany*

Accepted 2023 June 2. Received 2023 May 22; in original form 2022 September 13

ABSTRACT

We introduce the star formation and supernova (SN) feedback model of the SATIN (**S**imulating **A**GNs **T**hrough **I**SM with **N**on-Equilibrium Effects) project to simulate the evolution of the star forming multiphase interstellar medium (ISM) of entire disc galaxies. This galaxy-wide implementation of a successful ISM feedback model tested in small box simulations naturally covers an order of magnitude in gas surface density, shear and radial motions. It is implemented in the adaptive mesh refinement code RAMSES at a peak resolution of 9 pc. New stars are represented by star cluster (sink) particles with individual SN delay times for massive stars. With SN feedback, cooling, and gravity, the galactic ISM develops a three-phase structure. The star formation rates naturally follow observed scaling relations for the local Milky Way gas surface density. SNe drive additional turbulence in the warm ($300 < T < 10^4$ K) gas and increase the kinetic energy of the cold gas, cooling out of the warm phase. The majority of the gas leaving the galactic ISM is warm and hot with mass loading factors of $3 \leq \eta \leq 10$ up to $h = 5$ kpc away from the galaxy. While the hot gas is leaving the system, the warm and cold gas falls back onto the disc in a galactic fountain flow. The inclusion of other stellar feedback processes from massive stars seems to be needed to reduce the rate at which stars form at higher surface densities and to increase/decrease the amount of warm/cold gas.

Key words: methods: numerical – ISM: kinematics and dynamics – ISM: structure – galaxies: active – galaxies: ISM.

1 INTRODUCTION

Understanding the formation of galaxies within their cosmological context poses significant challenges owing to the large dynamical range in space and time as well as the wide range of physical mechanisms involved. In the current paradigm of galaxy formation, dark matter (DM) is gravitationally dominant on large scales, and is, therefore, crucial to the understanding of structure formation within the universe. Baryons follow the DM into gravitationally bound structures, the haloes, where they cool, which decreases their pressure and dissipates angular momentum (Binney 1977; Rees & Ostriker 1977; Silk 1977; White & Rees 1978). Eventually they form galaxies in their centre. Further cooling and fragmentation leads to the formation of Giant Molecular Clouds (GMCs) where stars form (McKee & Ostriker 2007). Feedback processes and outflows are needed to prevent stars from forming too efficiently compared to observations (e.g. White & Rees 1978). For low-mass galaxies, such effective feedback is thought to come from massive stars (Dekel & Silk 1986; Efstathiou 2000), whereas for high-mass galaxies, active galactic nuclei (AGN) feedback from supermassive black holes (SMBH) are likely the dominant source of feedback (e.g. Silk & Rees 1998; Benson et al. 2003).

It has been shown that feedback from massive stars, in the form of radiation, momentum, and thermal energy, can deplete cold-gas reservoirs, regulate star formation, and launch galactic winds in low-mass galaxies. Moreover, it is important in setting the phase structure and porosity of the multiphase ISM (e.g. Stinson et al. 2006; Dubois & Teyssier 2008; Sales et al. 2010; Ostriker & Shetty 2011; Dubois et al. 2014; Hopkins et al. 2014; Kimm & Cen 2014; Marinacci, Pakmor & Springel 2014; Vogelsberger et al. 2014; Gatto et al. 2015; Murante et al. 2015; Schaye et al. 2015; Wang et al. 2015; Martizzi et al. 2016). For a detailed review on this see Somerville & Davé (2015) and Naab & Ostriker (2017). There are various different stellar feedback channels. Radiation from massive stars can act directly to suppress star formation by ionizing and heating their immediate environment. Radiation feedback can additionally strengthen galactic outflows and thus help to lower the total gas content available to form stars (see e.g. Walch et al. 2012; Dale et al. 2014; Geen et al. 2015b; Peters et al. 2017; Kim & Ostriker 2018; Kim, Kim & Ostriker 2019, for some recent simulations). However, some authors find that the inclusion of strong radiation feedback suppresses galactic outflows by regulating star formation early on (Kimm et al. 2018; Smith et al. 2021). Stellar winds of

★ E-mail: rebekka.coles-bieri@uzh.ch

massive stars have been found to disperse their host cloud and suppress gas accretion onto the newly formed stellar cluster with various levels of efficiency (see e.g. Dale et al. 2014; Mackey et al. 2015; Gatto et al. 2017; Haid et al. 2018; Geen et al. 2021; Lancaster et al. 2021; Guszejnov et al. 2022, for most recent simulations). At the end of their lifetime, many massive stars explode as SNe, where an overpressurised gas bubble expands into, sweeps up, and accelerates ambient material. Depending on the larger scale environment they can eject gas from the galaxy and even the halo (see e.g. Kim & Ostriker 2015; Martizzi, Faucher-Giguère & Quataert 2015; Walch & Naab 2015; Walch et al. 2015; Haid et al. 2016; Martizzi et al. 2016; Li, Bryan & Ostriker 2017; Rathjen et al. 2021). An additional pressure component that can drive gas out of the ISM can come from cosmic rays that are generated in the SN blown shocks and interact with the magnetic field (Dorfi & Breitschwerdt 2012; Girichidis et al. 2016; Simpson et al. 2016; Girichidis et al. 2018; Hanasz, Strong & Girichidis 2021; Rathjen et al. 2021). Other sources of feedback such as the impact of stellar jets (Nakamura & Li 2007; Wang et al. 2010; Guszejnov et al. 2021; Verliat et al. 2022), high-energy photons from X-ray binaries (e.g. Kannan et al. 2016), as well as runaway stars (e.g. Kimm & Cen 2014; Andersson, Renaud & Agertz 2021; Steinwandel et al. 2022) are still a relatively new subject of exploration. These additional stellar sources of feedback are also found to have an impact on star formation as well as outflow properties. However, their respective relevance compared to other stellar feedback channels may be smaller and is still the subject of discussion. In order to better understand their relative importance and the details of their interaction with each other, some simulations also include various stellar feedback channels together within the same simulation (i.e. stellar radiation, stellar winds, cosmic rays, etc.; Dale et al. 2014; Geen et al. 2015a; Haid et al. 2018; Geen et al. 2021; Rathjen et al. 2021; Grudić et al. 2022). Such simulations are increasingly important and reveal how complex it is to properly understand their relative effect on the surrounding gas, star formation, and outflow properties.

For more massive galaxies, stellar feedback is, however, much less effective in regulating star formation because of their deeper potential wells that make it harder for the gas to escape. A more powerful source of feedback for these massive galaxies can be provided by AGN feedback from SMBHs that are thought to be ubiquitous at the centre of massive galaxies (e.g. Magorrian et al. 1998; Hu 2008; Kormendy, Bender & Cornell 2011). Rapid gas accretion onto black holes leads to an energy release capable of driving outflows that regulate star formation and the baryonic content of galaxies (Silk & Rees 1998). This, in turn, limits their own growth (leading to efficient self-regulation of the BH growth) as well as the gas content of the surrounding galaxy (Kormendy & Ho 2013). Although the general picture of black holes exerting feedback on their host galaxies is very attractive, the details remain vague, as the exact coupling between the AGN and the ISM of the host galaxy is still poorly understood. High-resolution simulations of different AGN feedback channels (jets, mechanically and radiation driven winds) have shown that including a multiphase gas structure results in different interactions with the ISM compared to simulations with a homogeneous setup (e.g. Bicknell et al. 2000; Sutherland & Bicknell 2007; Antonuccio-Delogu & Silk 2010; Wagner & Bicknell 2011; Gaibler et al. 2012; Bieri et al. 2017). Efforts in understanding the coupling efficiency of AGN feedback with the surrounding gas must therefore include a multiphase model of the ISM structure.

The multiphase ISM is composed of three different phases co-existing and interacting with each other: a *cold phase* consisting of atomic and molecular gas ($T < 10^4$ K); a *warm phase* ($T \sim 10^4$ K) composed of ionized gas and largely neutral gas; and a meta-stable *hot phase* (temperatures exceeding $T = 10^5$ K) of ionized gas produced predominantly by mechanical energy input from supernovae (SNe; Cox & Smith 1974; McKee & Ostriker 1977; Ferrière 2001; Klessen & Glover 2016). The ionized gas makes up most of the mass within the MW galaxy, followed by the cold and high-density molecular gas (see Saintonge & Catinella 2022, for a review). On the other hand, most of the volume is occupied by the warm neutral and ionized gas (e.g. Kalberla & Kerp 2009).

Turbulence is important for the structure of the ISM, as revealed by observations and simulations (see the review by e.g. Elmegreen & Scalo 2004; Mac Low & Klessen 2004). It is an important ingredient for star formation (McKee & Ostriker 2007) and affects the rate at which stars are formed (Federrath & Klessen 2012; Padoan et al. 2014) as well as influencing the global and local stability properties of galaxies (Romeo, Burkert & Agertz 2010; Hoffmann & Romeo 2012; Romeo & Agertz 2014; Agertz, Romeo & Grisdale 2015). Because turbulence dissipates on small scales, a mechanism of driving at large scales is needed. The main mechanisms that maintain turbulence within the ISM are, however, still not clear. There are several candidates capable of driving turbulence in the ISM: stellar feedback in the form of SNe, jets, winds and ionizing radiation (e.g. de Avillez & Breitschwerdt 2004; Joung & Mac Low 2006a; Kim, Ostriker & Kim 2013; Iffrig & Hennebelle 2015; Girichidis et al. 2016; Padoan et al. 2016); gravitational instabilities coupled with galactic rotation (Gammie, Ostriker & Jog 1991; Piontek & Ostriker 2004; Wada 2008; Bournaud et al. 2010; Renaud, Kraljic & Bournaud 2012; Krumholz & Burkhart 2016; Meidt et al. 2018; Nusser & Silk 2022); Magneto-Rotational-Instability (Balbus & Hawley 1991); as well as shear between a cold disc with respect to the hot halo (see discussion in Sec. 3 of Pfrommer et al. 2022). A multiphase model of the ISM gas structure must, therefore, go jointly with the development and understanding of a stellar feedback model that helps to regulate the (energetic) structure of the ISM. Additionally, the model of the galaxy ideally also includes the self-gravity of the gas as well as cooling channels that all influence the motion and evolution of the gas within the galaxy.

In recent years, there has been great deal of improvement in numerical simulations of the ISM and the interaction of the multiphase gas with various different stellar feedback channels as well as additional physical ingredients (see e.g. Kim & Ostriker 2015; Martizzi et al. 2015; Walch et al. 2015; Geen et al. 2015b; Peters et al. 2017; Rathjen et al. 2021). Such simulations reached ever higher resolutions to understand the various physical influences within a molecular cloud (MC) as well as their immediate surroundings. However, as a consequence of their detailed study of the different physical processes the simulations are performed in idealised setups and rarely include the larger galactic or even cosmological environment. Recent exceptions are dwarf galaxy simulations where the total gas mass is small enough to allow for a more detailed study (e.g. Hu et al. 2016, 2017; Emerick, Bryan & Mac Low 2019; Lahén et al. 2020; Rey et al. 2020; Gutcke et al. 2022).

Unlike detailed studies of dwarf galaxies or portions of the ISM, larger-scale simulations typically have to rely on sub-grid models to follow star formation, stellar feedback, and AGN feedback processes. Due to computational limitations, the internal structure of the multiphase ISM is, in those simulations, at best marginally resolved (e.g. Di Matteo, Springel & Hernquist 2005; Sijacki et al. 2007; Di Matteo et al. 2008; Booth & Schaye 2009; Dubois et al. 2012; Hopkins et al. 2014; Vogelsberger et al. 2014; Kimm et al. 2015; Schaye et al. 2015; Pillepich et al. 2018). The sub-grid models used are not expected to generally produce the same internal structure within a galaxy as those

found in resolved high-resolution feedback simulations. Despite this, larger-scale simulations remain valuable because they place galaxies in a more realistic environment, where major and minor mergers, gas clump capture, as well as cold filamentary accretion affect the evolution of these galaxies, likely in a way that is not predicted by idealised simulations. Despite the simplicity of their modelling, these large-scale studies have highlighted the capacity of stellar and AGN feedback to regulate the star formation process as well as gas content in small and massive galaxies, respectively.

The main limitation of these large-scale simulations is numerical resolution as much higher resolution is required to attempt to model the ISM (see e.g. Kim & Ostriker 2015; Martizzi et al. 2015; Walch et al. 2015; Geen et al. 2015b; Peters et al. 2017; Rathjen et al. 2021). Simulations of MW-like galaxies that start to bridge the gap between such large-scale models and more detailed simulations of the ISM and individual MCs have only recently started to become numerically feasible (Agertz et al. 2013; Rosdahl et al. 2015; Grisdale et al. 2017; Hopkins et al. 2018; Marinacci et al. 2019; Martizzi et al. 2019; Tress et al. 2020). However, such simulations have not (yet) studied the interaction of AGN feedback with the surrounding multiphase ISM. But in order to properly quantify the role of AGN in the evolution of (massive) galaxies we need more theoretical work involving realistic simulations of AGN feedback interacting with the surrounding turbulent and multiphase ISM structure. Usually sub-grid models rely on a number of assumptions regarding the coupling between the wind, jet, or radiation with the gas. Such sub-grid models are not expected to generally produce the same results as those found in resolved high-resolution AGN feedback simulations. With an increasing number of simulations that manage to resolve more of the the multiphase structure of the ISM, it becomes important to also ensure that AGN feedback models correctly bridge the gap between large and small scales. It is therefore time for new simulations that will use a physically validated approach in modelling AGN feedback to properly understand the interaction with the multiphase gas and how exactly AGN feedback drives large-scale winds. Such simulations then can contribute to a better understanding of how hydrodynamical sub-grid models can be improved in light of the results. Because the properties of the ISM are so tightly linked to star formation and stellar physics, the effort must go hand-in-hand with the development of a stellar feedback model that regulates star formation as well as the properties of the ISM such that it matches with observations.

The goal of the **SATIN** (**S**imulating **A**GNs **T**hrough **I**SM with **N**on-Equilibrium Effects) project is to improve our understanding of the detailed interaction of the AGN with the turbulent multiphase gas and how large-scale winds are driven. The entire galactic MW disc simulations have sufficient resolution to capture a distinct multiphase ISM with the different gas phases interacting with each other. The simulations cover an order of magnitude in gas surface density, and naturally takes into account shear and radial motions.

This is the first paper of the project where we present the initial building blocks of the simulations, in particular the star formation model via sink particles as well as the SNe feedback implementation. The SATIN model incorporates a star formation and stellar feedback model that has been successfully tested in stratified solar neighbourhood-like simulations (Walch et al. 2015, see) and that we adapted to the adaptive mesh refinement (AMR) code RAMSES (Teyssier 2002). The SNe feedback model uses a stellar evolution model and single star tracking to get individual SN delay times for the massive stars. Additionally, it adaptively adjusts to the local environment of each SN explosion by switching between the injection of thermal energy and momentum depending on the surroundings. We then test in this paper the model in a full self-gravitating MW-like disc galaxy simulation, quantify the interaction of the SNe with the multiphase and turbulent ISM, and compare the results with observations. Only once we established that the used stellar feedback model fulfils our requirements of regulating the properties of the gas within the galaxy as well as star formation we then go forward and analyse in detail the interaction of the AGN with the simulated galaxy. This will be subject of future papers.

The paper is structured as follows: In Section 2, we introduce the first building blocks of the SATIN model and then explain in Section 3 the simulation setup of the isolated self-gravitating turbulent MW-like disc galaxy that we simulate with and without SNe feedback. In Section 4, we first give a qualitative overview of the global evolution and morphology of the simulations. We then describe the star formation rates of the galaxies and compare them against observations in Section 4.2. In Section 4.3, we then investigate the multiphase ISM structure and the mass and volume-filling factors of the gas within the galaxy. Furthermore, we look at the turbulent structure of the ISM in Section 4.4 and quantify the galactic outflows in Section 4.5. In Section 5, we discuss the results of our simulations in the context of other studies as well as possible caveats. Finally, this paper is summarised and concluded in Section 6. In Appendix C, we describe in more detail the calculations of the power spectra presented in this paper.

2 SATIN MODEL

In this Section we introduce the first incarnation of our SATIN model that we use to study the ISM within a simulated MW-like galaxy. The model is a galaxy wide implementation of a ISM feedback model tested in small box simulations (see Walch et al. 2015) and adapted to the AMR code RAMSES (Teyssier 2002). We will begin with a summary of the numerical methods used to model gravity and hydrodynamics (Section 2.1). Then we describe the physical models such as non-equilibrium cooling (Section 2.2), the formation of massive stars (Section 2.3 and 2.4), a stellar stellar evolution model to track the age and death of the massive stars (Section 2.5), and the implementation of SN feedback with individual delay times (Section 2.6).

2.1 Numerical methods

For the simulations, we use the AMR hydrodynamics code RAMSES. The code solves the poisson equations for collisionless particles (DM, stars, sinks) coupled to the hydrodynamics of an inviscid fluid via an AMR finite volume method. The motions of the collisionless particles are evolved through the gravitational force with an adaptive particle mesh solver using a cloud-in-cell interpolation, taking into account the mass contribution from the gas (Guillet & Teyssier 2011). The gas is modelled with a second-order unsplit Godunov scheme. We use the HLLC Riemann solver (Toro, Spruce & Speares 1994) with MinMod total variation diminishing scheme to reconstruct the interpolated variables from their cell-centred values. To relate the pressure and internal energy, we use an adiabatic index of $\gamma = 5/3$. Throughout the simulations, we use outflow (i.e. zero gradient) boundary conditions on all sides.

2.2 Non-equilibrium cooling

The gas temperature and the non-equilibrium ionization states of hydrogen and helium are tracked using the RAMSES-RT radiative hydrodynamics (RHD) extension to RAMSES. In the simulations

presented, we only use the chemistry module of RAMSES-RT and no photons are created and transported. The details of this method, in particular the ionization chemistry, are given in Rosdahl et al. (2013) but we summarize the processes here. We assume a hydrogen mass fraction of 0.76 and a helium mass fraction of 0.24. The cooling and heating rates include collisional ionization and excitation (Cen 1992) and formation of hydrogen and helium by recombination (Hui & Gnedin 1997). Also included are Bremsstrahlung cooling (Osterbrock & Ferland 2006), dielectric recombination (Black 1981) and Compton electron scattering off cosmic microwave background photons (Haiman, Rees & Loeb 1996). We include hydrogen and helium photo-ionization and heating from a UV background at redshift zero (Faucher-Giguère et al. 2009). Additionally we enforce an exponential damping of the UV radiation above the self-shielding density of $n_{\rm H} = 10^{-2}$ cm^{-3}. For the gas with temperatures above 10^4 K, the contribution to cooling from metals is added using CLOUDY (Ferland et al. 1998) generated tables. It assumes photoionization equilibrium with a redshift zero UV background (Haardt & Madau 1996). Below a gas temperature of 10^4 K, we use fine structure cooling rates from Rosen & Bregman (1995) that allow the gas to radiatively cool down to 10 K. The thermochemistry of molecules is not included in the public version of RAMSES-RT that we use. As described below, we initialize the galaxy with a uniform solar metallicity ($Z = 0.014$; Lodders, Palme & Gail 2009) and place no metals outside the disc. The initial turbulence-driving SNe (described below) release 2 per cent of the injected mass as metals. During the simulations, the stars release no metals within their lifetime, nor when they explode in a SN (i.e. we assume zero stellar yields).

2.3 Sink formation

Once a molecular cloud is formed and accumulated enough mass it collapses and forms stars and star clusters. We employ collisionless sink particles to model the formation of internally unresolved star clusters in dense regions that undergo gravitational collapse. To find the formation sites of the sink particles, we detect high-density clumps by running a clump finder (Bleuler & Teyssier 2014) at every global time-step. This method identifies all peaks and their highest saddle points if the density of the gas cell is above a set threshold density (i.e. $\rho_{\rm sink} = 50$ H cm^{-3}). When the peak-to-saddle ratio is greater than 1.5, we recognize a clump as an individual entity, whereas otherwise we merge the density peak with the neighbour peak with which it shares the highest saddle point. We then investigate the gas surrounding the density peak for gravitational collapse. We form a sink particle if a number of requirements are met. First, we perform a virial theorem type analysis to ensure that the gravitational field at a possible location for sink formation is strong enough to overcome internal support of the gas within the clump. This avoids forming sinks in gas which is only compressed by thermal pressure rather than gravity. Secondly, we ensure that the requirement for a converging flow ($\nabla \cdot \boldsymbol{v} < 0$) is met (similar to Federrath et al. 2010), ensuring that the gas within the accretion volume contracts at the moment of formation. Finally, we do not allow the accretion radius to overlap with that of another existing sink (similar to Federrath et al. 2010). If these conditions are met, we form a sink particle. During the length of the simulation the sink particles do not merge and remain individual entities. Similar approaches have been used in stratified ISM simulations (Gatto et al. 2017; Rathjen et al. 2021) or idealised molecular cloud simulations (Iffrig & Hennebelle 2015; Geen et al. 2018, 2021).

Once a sink particle is formed it can, at each time-step, accrete gas from cells which are within their accretion radius ($R_{acc} = 2 \times \Delta x$) and whose density is greater than the threshold density for formation. Additionally, we require the gas in a cell to fulfill the same conditions as for sink formation. Here Δx is the distance from the sink to the cell centre of adjacent cells. Note, that we enforce the highest refinement within a sphere with radius $R_{\rm res} = 6 \times \Delta x$ centred around each sink particle, ensuring that the accretion region has a well defined shape and that the SNe expands into a maximally refined region.

If the requirements are met the accreted gas mass from a cell is

$$\Delta m = \max\left(0.5(\rho - \rho_{\rm sink})(\Delta x)^3, 0\right), \quad (1)$$

where ρ is the mean density within the accretion region. At each time-step, the accreted mass is added onto the sink such that mass, linear momentum, and angular momentum are conserved (see appendix B in Federrath et al. 2010, for a more detailed discussion of angular momentum conservation). The density within each cell in the accretion region is lowered by the ratio of the accreted mass over the volume of the accretion region. The accreting sink is, in addition, moved to the centre of mass of the particle-gas configuration before the accretion step. The code accounts for overlapping accretion regions by reducing the corresponding weight of the accretion mass considering the volume of the overlapping regions. All the formed sink particles stay active throughout the whole simulation time.

The formation and accretion of gas onto a sink particle at the chosen density will reduce the local density and ensures that the Jeans length is resolved for most of the gas cells within the simulations. This helps avoid artificial collapse of the molecular cloud (Truelove et al. 1997).

The sink particles are evolved through the gravitational force with a particle mesh method already present in RAMSES for the DM particles (see Section 2.1). Using this method is desirable due to the large number of sink particles in our simulations.

2.4 Massive star formation

Typically sink particles are introduced to represent gravitationally collapsed objects whose physical size is below the grid scale by orders of magnitude. In our simulations the formed sink particles are considered to be tracing star clusters and we use them to trace the most physical location for star formation within the star cluster. We track the mass of every sink particle, which we then define as the cluster mass. We are only interested in the evolution of massive stars (i.e. stars above 9 M$_\odot$) as those stars have sufficient mass to generate a core collapse SN (see e.g. Díaz-Rodríguez et al. 2018; Díaz-Rodríguez et al. 2021).[1] There is, indeed, no clear cut-off for winds and radiation as all stars produce some winds and UV radiation, but the amount of radiation from these stars drops significantly as the mass of the stars decrease (see for instance Leitherer et al. 1999). This will only be important for future work. To follow the evolution state of such massive stars that form within the star cluster we implement a sub-grid model.

First, we assume that all gas accreted onto the sink particles is converted into stars. Each sink particle (star cluster) tracks the amount of mass accreted onto it and every time this exceeds 120 M$_\odot$ for an individual sink particle we create a virtual object representing a massive star of mass M and attach it to the corresponding sink particle. We then decrement the accretion mass by 120 M$_\odot$ and repeat the process. By subtracting 120 M$_\odot$ rather than the mass of the stellar object, we account for the stars below 9 M$_\odot$ in the mass distribution of the sink. We do not follow the low-mass stars individually and

[1] Binary evolution may significantly complicate this.

thus assume that they do not emit any winds, radiation, or explode in a SNe. The star itself is a virtual object that moves with the sink and the number of massive stars associated with each sink differs. The minimal, typical, and maximal mass of the sink particles formed within the simulation are 10 $M_\odot$, $10^{5.5}$ Msolar, and $10^{7.5}$ Msolar, respectively. The object itself tracks the initial mass and age of the star, that is then used by the stellar evolution and feedback model described in the next Section. The initial mass of every new-born star is drawn from a Salpeter IMF (Salpeter 1955) within a mass range of 9–120 $M_\odot$. The same model specifics have been used in Gatto et al. (2017) and Peters et al. (2017) for stratified ISM simulations. A similar implementation can be found in Iffrig & Hennebelle (2015) and Geen et al. (2018).

2.5 Stellar evolution

We follow the stellar evolution of the massive stars by tracking the age of the star associated to a sink particle (star cluster) in order to get realistic SNe delay times for each individual star within the star cluster. We use the stellar evolution tracks (Ekström et al. 2012) from the zero-age main sequence (ZAMS) with a rotation rate $vini/v_{crit} = 0.4$. The evolution is computed until the Wolf-Rayet/pre-SN phase. As already done in Gatto et al. (2017) we store a grid of 112 tracks for stars in the mass range of 9–120 $M_\odot$, separated by 1 $M_\odot$. We interpolate linearly between tracks for each individual star. We make the simplified assumption that each formed massive star immediately starts with the ZAMS evolution and thus do not account for a delay time due to star formation or a proto-stellar phase (see Grudić et al. 2022 as well as Verliat et al. 2022 for simulations that includes protostellar jet feedback). We presume that each massive star explodes as a Type II SN once it has reached the end of its lifetime. The lifetimes of the massive stars range from 35 Myr for the least massive star (9 $M_\odot$) to 3.5 Myr for the most massive star (120 $M_\odot$) in our sample.

The energy released by a single SN event ($E_{SN} = 10^{51}$ erg) is injected into the surrounding of the sink particle in the form of thermal energy or momentum input, depending on whether the adiabatic phase of the SN remnant is resolved (see the next section for detailed information). We also add the mass of the SN progenitor to the injection region and decrement the total mass of the sink by the same amount. We assume zero stellar yields and release no metals during the SNe explosion.

In the SATIN model we do not account for the unresolved stellar remnants or runaway stars (see Andersson, Agertz & Renaud 2020 and Steinwandel et al. 2022 for a detailed study of the effect of runaway stars). Moreover, we did not include Type Ia SNe explosions originating from an old stellar population.

2.6 SN energy and momentum input

The implemented SN model uses the individual delay times from the stellar evolution model and adaptively adjusts to the local environment of each SN explosion and switches between the injection of thermal energy and momentum depending on the surroundings. We release thermal energy of $E_{SN} = 10^{51}$ erg to the neighbouring cells of the star provided that the adiabatic phase of the SN remnant is resolved. If, however, the density in the injection region is high and the Sedov–Taylor phase is unresolved, we switch to a momentum input scheme based on Blondin et al. (1998).

Differentiating the injection method based on the local cooling length has been already used in previous studies such as (Hopkins et al. 2014; Kimm & Cen 2014; Kim & Ostriker 2015; Martizzi et al. 2015; Gatto et al. 2017, to name a few).[2]

In our implementation, we distribute the thermal energy or momentum, for both models, in a volume weighted fashion within a sphere of radius $R_{inj} = 2 \times \Delta x$. Note, that the high resolution region around the star is larger (i.e. $R_{res} = 6 \times \Delta x$) and that the SNe thus expands into a maximally refined region independent of the surrounding density. By doing so, we additionally avoid the problem of dealing with coarse-fine boundaries between two refinement levels.

We assume that each SN remnant ejects the mass of the progenitor star into its surroundings and each cell in the injection region thus receives momentum associated to the deposition of the ejecta from a star that moves with respect to the mesh. In order to decide whether we inject thermal energy or momentum we first calculate the mean local hydrogen number density n_H in the region within the injection radius and then calculate the radius of the bubble at the end of the Sedov–Taylor phase as done in Blondin et al. (1998):

$$R_{ST} = 19.1\, E_{51}^{5/17}\, n_H^{-7/17}\ \mathrm{pc}, \tag{2}$$

where $E_{51} = E_{SN}/(10^{51}\mathrm{erg})$ is the number of SNe exploding at the given time. If $R_{ST} < R_{inj} = 3\Delta x$, we inject momentum rather than thermal energy. This ensures that, if we inject thermal energy, the local cooling radius is sufficiently resolved by at least three resolution elements along each Cartesian axis (see also Kim & Ostriker 2015 and Martizzi et al. 2015 for a discussion about this).

After the injection of thermal energy or momentum we update the time-step within the simulation using the Courant–Friedrich–Levy stability condition (Courant, Friedrichs & Lewy 1928), where the time-step cannot be larger than

$$\Delta t = C_{CFL} \frac{\Delta x}{\max\left(|v| + c_s\right)}. \tag{3}$$

Here Δx is the cell width, v the gas velocity, c_s is the sound speed, and C_{CFL} is the Courant number, where we used $C_{CFL} = 0.5$ in our simulations. This is done in order to best capture the evolution of the blast wave. We will now explain the two injection schemes in more detail.

2.6.1 *Thermal energy input*

If the SN is resolved we inject the total energy of $E_{SN} = 10^{51}$erg per SN to all the cells within the injection radius (i.e. $R_{inj} = 2 \times \Delta x$). The thermal energy in each cell of the injection sphere is therefore updated as

$$\epsilon_{th,cell} = E_{SN}/V_{fb}, \tag{4}$$

where V_{fb} is the volume of all the cells within the injection region.

Along with the thermal energy we also inject the ejected gas mass, while conserving momentum, into the cells within the same region. Here, we assume that each SN remnant ejects the mass of its progenitor star into the surroundings. And, finally, we update the total energy of the gas cell taking into account the changes to the thermal and kinetic energy.

This can increase the temperature of a cell up to $\sim 10^8$ K in a low-density medium where the injected mass is much higher than the mass of the surrounding. The overpressured gas then expands

[2]See appendix of Kimm & Cen (2014) for a more detailed discussion on the differences between their method and the implementation of Hopkins et al. (2014).

into the ambient, inhomogeneous, ISM gas as a Sedov–Taylor blast wave. In principle about ∼30 per cent of the total thermal energy can be deposited into kinetic energy (Chevalier 1974). However, as is already well known (Katz 1992; Navarro & White 1993; Abadi et al. 2003; Slyz et al. 2005; Stinson et al. 2006; Creasey et al. 2011; Hummels & Bryan 2012; Kimm & Cen 2014) the atomic and metal cooling processes in the gas can rapidly radiate the internal energy away before the blast wave sweeps up the ambient medium in dense environments or in simulations where the cooling radius is underresolved. This is why we switch to a momentum-input scheme in situations where the cooling radius is unresolved.

2.6.2 *Momentum input*

In the case of an unresolved Sedov–Taylor phase of the SN remnant, we follow a momentum-input scheme. The input momentum is at solar metallicity calculated as (Blondin et al. 1998; Thornton et al. 1998; Kim & Ostriker 2015; Geen et al. 2015a)

$$p_{\rm ST} = 2.6 \times 10^5 E_{51}^{16/17} n_{\rm H}^{-2/17} {\rm M}_\odot {\rm kms}^{-1}. \quad (5)$$

We inject the momentum taking into account that each progenitor star particle moves with respect to the mesh, and we assume that each SN remnant is spherically symmetric in the frame of reference of the progenitor star. We further assume that the centre of each SN is the position of the parent sink particle associated with the exploding progenitor star. The injected momentum is calculated using a velocity of

$$v_{\rm inj} = \frac{p_{\rm ST}}{M_{\rm inj}} \hat{r}, \quad (6)$$

where $M_{\rm ej}$ is the ejected SNe mass (i.e. mass of progenitor star), and $\hat{r}$ is a unit vector that points from the sink particle position towards the centre of the cell into which we inject the velocity. The velocity $v_{\rm inj}$ thus points radially outwards. Along with the momentum from the SNe, we also add the ejected gas mass into the cells, again while conserving momentum. And as in the thermal-energy implementation we also change the total energy of the system taking into account the changes to the thermal and kinetic energy.

3 SIMULATION SETUP

We explore our model in high-resolution simulations of an isolated self-gravitating turbulent MW-like disc galaxy to naturally account for shear and radial motions. To test the effect of the SNe in regulating star formation and on the simulated multiphase ISM, we run the galaxy with (*SNe*) and without SNe feedback (*nSNe*). We collectively refer to both simulations as the SATIN1 simulations. The simulated galaxy consists of a disc of gas and stars, a stellar bulge, and a DM halo. After two initialization stages described below, we use a sink formation algorithm to model the formation, evolution and eventual SNe explosion of massive stars within the star cluster using stellar tracks.

3.1 Initial conditions

We study an isolated self-gravitating turbulent MW-like galaxy made of a disc of gas and stars, a stellar bulge, and a DM halo. The initial conditions are set-up with the initial condition code DICE (Perret 2016). The DM halo initially follows an NFW (Navarro, Frenk & White 1996) density profile with a concentration parameter of $c = 22$. The virial velocity of the DM particles is set to be $v_{200} = 134$ km s^{-1}, which corresponds to a virial radius of $R_{200} \approx 190$ kpc and a virial mass of $M_{200} = 79 \times 10^{10}$ M$_\odot$. With a cutoff radius of 12 kpc the total mass of the DM halo is 3.6×10^{11} M$_\odot$. We use 10^6 DM particles to sample the halo.

The total stellar mass of the galaxy is 4.6×10^{10} M$_\odot$ and the total gas mass of the galaxy is 0.59×10^{10} M$_\odot$, resulting in an initial gas fraction within the galaxy of $f_{\rm gas} = 0.12$. The stellar and gas disc follow an exponential and sech-z profile with a scale length of 6 kpc and scaleheight of 0.4 kpc. The stellar bulge with a total mass of 1.2×10^{10} M$_\odot$ follows a Hernquist profile (Hernquist 1990) of scale radius 2 kpc. We use 1.5×10^6 and 2×10^5 star particles to sample the disc and bulge, respectively. The stellar mass resolution is 2.7×10^4 M$_\odot$.

The galaxy is initialized with a uniform solar metallicity ($Z = 0.014$; Lodders et al. 2009) and no metals are placed outside the disc. As described below, the initial turbulence-driving SNe release 2 per cent of the mass as metals. The circumgalactic medium (CGM) initially consists of a homogeneous hot and diffuse gas with a constant hydrogen number density of $n_{CGM} = 10^{-6}$ H cm^{-3}, temperature $T = 10^6$ K, and zero metallicity.[3] The advection of metals is tracked as a passive scalar on the AMR grid.

Before we turn on all the physics discussed in detail above (Section 2) we go through two initial phases; a relaxation phase and turbulence injection phase. In the relaxation phase we allow the galaxy to relax to an equilibrium configuration (with a reasonable disc thickness) for 50 Myr. We perform this first phase without gas cooling, sink formation, and feedback. It allows removing signatures from the imperfect equilibrium of the initial conditions. After this first relaxation phase we turn on gravity and gas cooling and randomly explode stars for another 10 Myr to inject additional turbulence and to prevent the galaxy from collapsing into a thin disc (similar approach has been used in Hu et al. 2016). Specifically, we inject 10^{51} erg of thermal energy at a random location within the whole stellar disc and bulge. The rate is calculated using the gas surface density of the galaxy, assuming a Kennicutt–Schmidt (KS) relation (Kennicutt 1998a), and an efficiency parameter for the SNe to explode of $\epsilon_{\rm SN} = 0.02$. Note, that the rate at which the SNe explode within this initial turbulence phase is in the same spirit as the often used star formation recipe based on the Schmidt law (Schmidt 1959; Cen & Ostriker 1992; Katz 1992). In addition to momentum and energy, the initial turbulence-driving SNe explosions also inject 2 per cent of the mass in metals. Only after these two stages we turn on sink formation to follow the formation and evolution of the star clusters formed within our galaxy self-consistently. The stars set in the initial condition of the galaxy contribute only to the dynamical evolution and gravitational potential of the rotating disc, but they never explode as SNe.

3.2 Adaptive refinement

The box size is 650 kpc with the coarsest level of 9 and a maximum level of 16 corresponding to a minimum cell size of 9 pc for most of the galaxy. For refinement we employ a quasi-Lagrangian scheme where a cell is refined if the gas within a cell is larger than 5×10^3 M$_\odot$ or if the cell has eight or more DM and/or star particles within the cell. Additionally, we also refine at each level if the cell size exceeds 80 per cent of the local Jeans length, until the region reaches the maximum resolution of 9 pc (corresponding to level 16). Note that at maximum resolution, the Jeans length can become underresolved

[3]Most of the SNe explode in our simulation within the starforming ISM. Setting the metallicity to zero within the CGM is, therefore, not an issue for understanding the impact of SNe on the structure and energetics of the ISM.

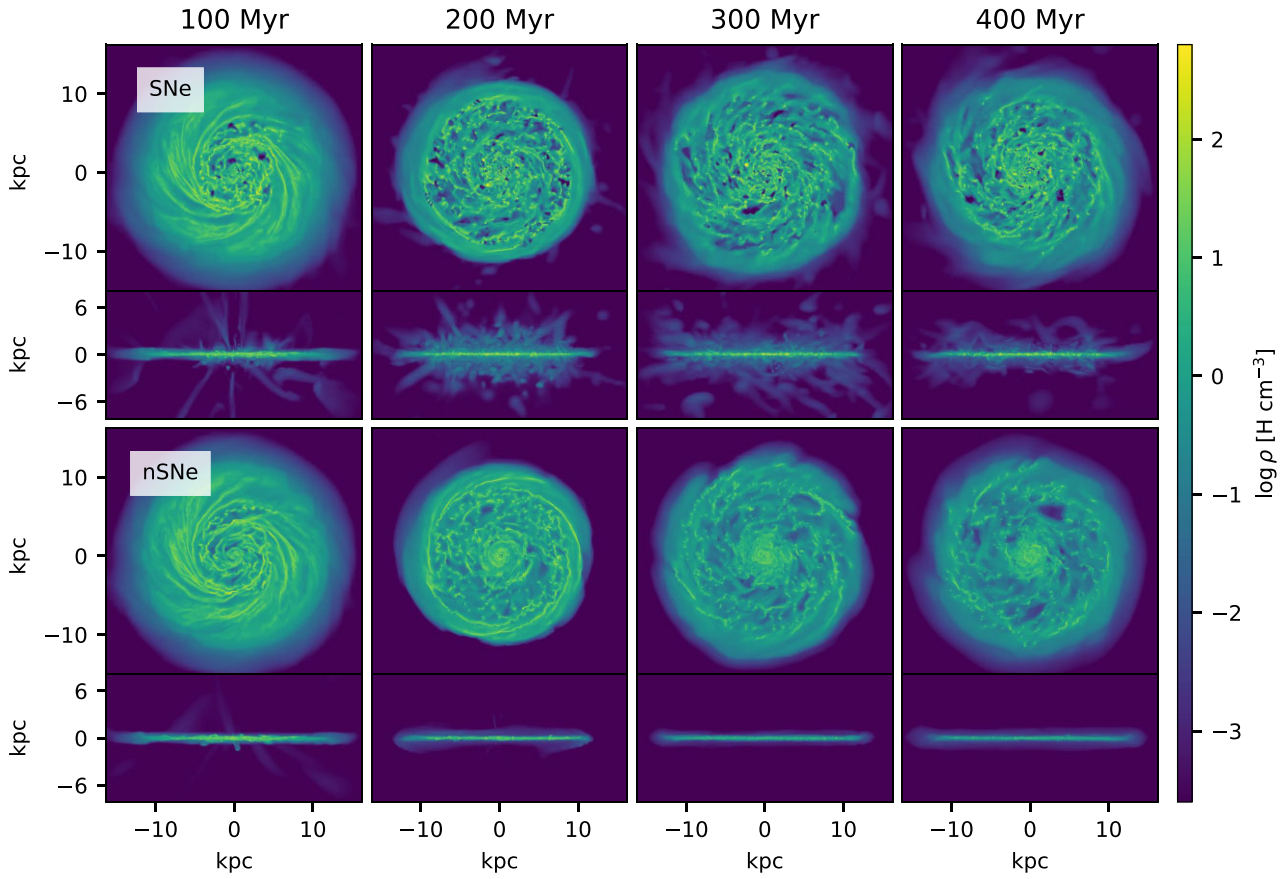

Figure 1. Gas density maps (mass-weighted) of the *nSNe* (top panel) and *SNe* (bottom panel) simulation for different times ($t = 100$, 200, 300, 400 Gyr) from the left- to right-hand side. Each panel shows both face-on (32×32 kpc, upper part) and edge on (32×16 kpc, lower part) views. The pixel size is taken to be $dx = 10$ pc. The appearance of the ISM is smoother and no cavities of lower densities are visible in the *nSNe* simulation due to the lack of SNe. SNe create a multiphase ISM structure within the whole disc and pushes the gas a few kpc above and below the disc plane increasing the disc thickness.

for a few cells which can lead to artificial collapse of self-gravitating gas (Truelove et al. 1997). We thus set the sink formation density threshold to a value (i.e. $\rho_{\rm sink} = 50\,{\rm H\,cm^{-3}}$) at which the Jeans length becomes resolved by less than 4 cells in gas with temperatures below 200 K at the highest refinement level (see also Section 2.3). Forming stars from this high-density gas will reduce the local density and ensures that the Jeans length is resolved for most of the gas cells. Note that for a majority of the cells refinement is triggered due to the gas mass scale rather than due to the Jeans length criteria. This causes the galaxy to have much more refined cells than if only the Jeans criterion is used. In addition, we also enforce the highest refinement within a sphere with radius $R_{\rm res} = 6 \times \Delta x$ centred around each sink particle, ensuring that the SNe expands into a maximally refined. We found that these two additions are important for the SNe to be properly resolved as it ensures that the gas around the star is also in a highly resolved region.

4 RESULTS

In this section, we discuss two simulated galaxies run with (*SNe*) and without (*nSNe*) SNe feedback. Both galaxies start with identical initial conditions. We explore the ability of the SATIN model to regulate star formation and look whether or not the galaxy manages to reach a self-regulated steady state (Sections 4.2 and 4.3). To understand where the SATIN model reasonably regulates the formation of stars we will also compare the simulations with observational data. Further, we will investigate the multiphase ISM structure of the two simulations and examine the impact of the SNe on the structure (Section 4.3) and energetics (Section 4.4) of the ISM. Finally, we discuss the gas dynamics and flows (Section 4.5).

4.1 Qualitative differences

The evolution of the two simulated galaxies, *SNe* and *nSNe*, are visually different from each other. Fig. 1 shows the evolution of the gas density maps for the two different simulations. The initial 22 Myr of evolution are, after the two initialization phases, identical for the two simulations. The simulations begin to diverge only once the first SN explodes and low-density pockets appear due to the effect of the expanding SNe bubbles.

Stars form predominantly where the density is the highest such as the central region and along the spiral pattern in the gaseous disc. The first SNe explode in these high-density regions, carving out cavities of low-density gas, and destroying the gaseous spiral pattern within the galaxy (see evolution of the *SNe* run in the lower panel of the figure). After the first 200 Myr, the gas distribution of the *SNe* run becomes increasingly structured again. This is because at that stage the SFR is decreasing and thus there are less SNe disturbing the gas distribution which allows the gas to settle more. Dense and cold gas regions within which star clusters form are surrounded by hot, lower density gas and a multiphase ISM develops. Gas bubbles are pushed out by the SNe from the star-forming disc into the halo. As we will

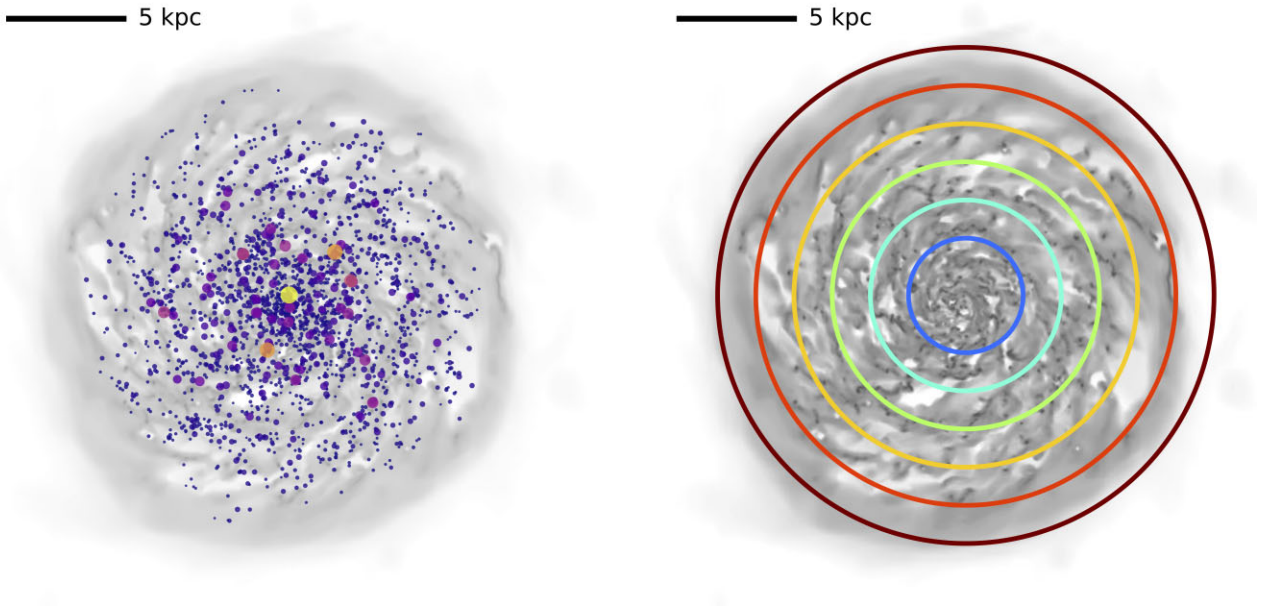

Figure 2. Left-hand panel: sink distribution within the galaxy at $t = 350$ Myr for the *SNe* simulation plotted over the corresponding gas density distribution. The size of each point is scaled with the mass of the star cluster where more massive stellar clusters appear larger. The colour of the points changes from blue (low mass star clusters of 10^7 $M_\odot$) to yellow (high mass star clusters of 10^7 $M_\odot$). We chose the colour and point size to best highlight structures within the galaxy. For instance, a spiral structure within the star cluster distribution starts to emerge in the outer regions of the galaxy. Within the centre the star cluster distribution appear more chaotic. Right-hand panel: gas distribution (mass-weighted) for the *SNe* simulation at the same time $t = 350$ Myr. Overplotted are concentric rings ($r = 3, 5, 7, 9, 11, 13$) in the same colours as used in Fig. 6.

see, part of the gas falls back onto the disc while some gas escapes the galaxy.

Comparing the two runs in Fig. 1, we observe that the gas in the *SNe* simulation reaches both higher and lower density extremes. Due to the lack of SNe, the appearance of the ISM in the *nSNe* simulation is smoother and no large cavities are visible. Continued gas accretion onto the stellar clusters (sinks) removes gas from within the disc and leads to star formation within the cluster. This alone already helps to form structures within the ISM, as seen in the *nSNe* simulation. The central region of the *nSNe* simulation accumulates more gas over time, whereas SNe explosions disrupt the central region of the galaxy and create a multiphase structure in the centre.

The edge-on view show that in the *SNe* simulation gas flows out of the galaxy and the SN feedback increases the disc thickness compared to the *nSNe* simulation where the galaxy develops into a razor-thin disc. In comparison, with SNe feedback the disc thickness[4] of the warm/cold gas at 100, 200, and 300 Myr changes between 3.2/0.9 and 4.6/1.1 and 4.8/1.2 kpc, respectively. Whereas, the thickness of the warm/cold gas in the *nSNe* simulation is marginally changing around 1.4/0.3 kpc – less than half the thickness of the *SNe* simulation. The large-scale outflows generated by the SN explosions push the gas to a few kpc above and below the disc plane. The outflows correlate with star formation and start in the central region of the galaxy where the first stars are born. At later times (200 Myr) when star formation also reaches the edge of the galaxy, outflows escape from the full disc plane (see Section 4.5 for a quantitative discussion on the gas flows).

[4]We measure the thickness to be the position where the first local minima of the vertical density profile is less than 20 per cent of the maximum density within the disc.

Fig. 2 shows on the left side the sink distribution within the galaxy at $t = 350$ Myr for the *SNe* simulation (overplotted onto the density distribution). The point size is weighted by the mass of the star cluster. The colour of the points changes from blue (low-mass star clusters of $\sim 10^3$ $M_\odot$) to yellow (high-mass star clusters of 10^7 $M_\odot$). The size and colour distribution shows that the high mass clusters are mostly around the centre of the galaxy where the first stars form. A spiral structure in the star cluster distribution starts to emerge in the outskirts of the galaxy. On the right side the gas distribution is shown for the same snapshot and same size. Overplotted are circles ($r = 3, 5, 7, 9, 11, 13$) in the same colours used in Fig. 6. We will use the same ring radii for different analyses later on.

The face-on temperature slices in Fig. 3 at $t = 350$ Myr show a complementary picture to the density maps. The densest regions contain the lowest temperatures for both the *SNe* and *nSNe* simulation, whereas the highest temperatures can be seen in the low-density regions within the galaxy. A distinct three-phase ISM with cold ($T < 300$ K), warm ($T = 300$–(2×10^5) K), and hot ($T > 2 \times 10^5$ K) gas is visible in the *SNe* simulation for most of the galaxy. The gas structure outside $\sim$9 kpc is at $t = 350$ Myr still very smooth and cold. In this outer region the gas did not yet form a multiphase structure. The hot gas in the *nSNe* simulation originates from the initial SN explosions used to inject additional turbulence and to prevent the galaxy from collapsing into a thin disc. In the *SNe* simulation, the gas cavities carved by the accreting sinks as well as SNe feedback is filled with shock-heated gas around 10^7 K. It is still possible that part of this hot gas also originates from the hot surrounding medium around the galaxy. Given that the ratio of outflow versus inflow rates (OFR/IFR) discussed in Section 4.5 is well above one for the majority of the simulation, we assume that this is, however, a small amount.

A large portion of the low-density hot gas is also pushed outside the disc by the SN explosions. The temperature slice for the *SNe*

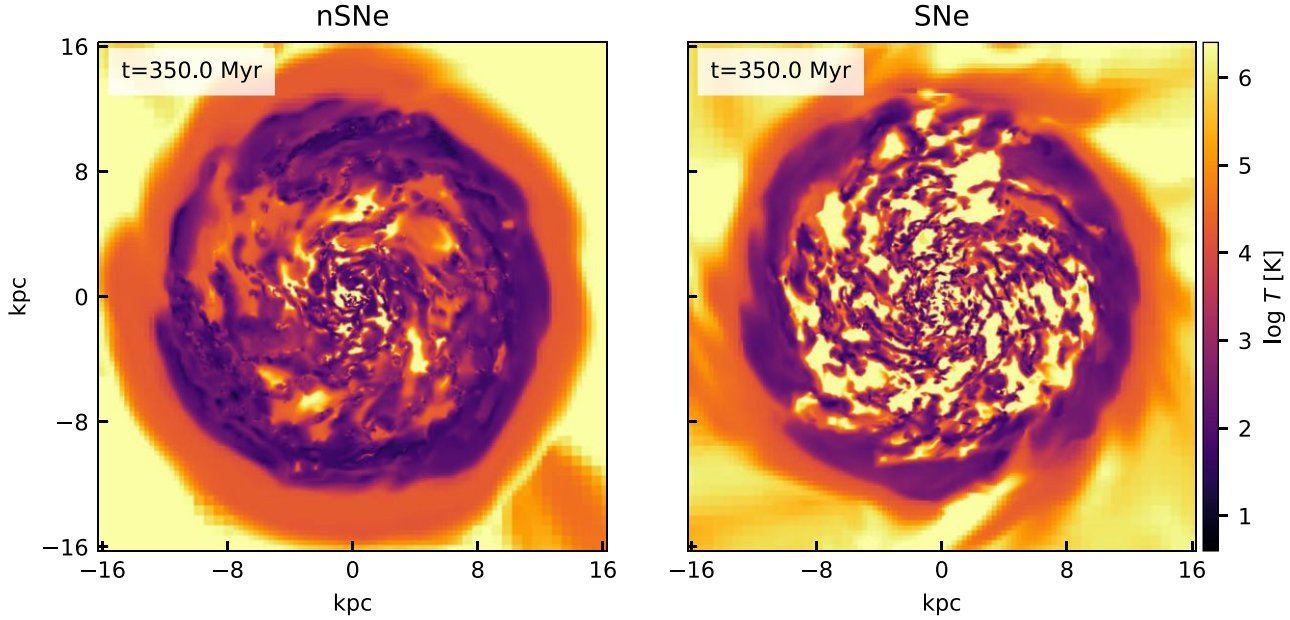

Figure 3. Face-on density-weighted gas temperature slice of the *nSNe* (left-hand panel) and *SNe* (right-hand panel) at $t = 350$ Myr. The map scale and pixel size is as in Fig. 1. The hot gas cavities in the *SNe* simulation is filled with shock-heated gas around 10^7 K. A distinct three-phase ISM is visible in the *SNe* simulation. The dynamical evolution of the *nSNe* creates holes that is filled with hot gas from the surrounding. More volume is filled by the warm than hot gas for the *nSNe* simulation.

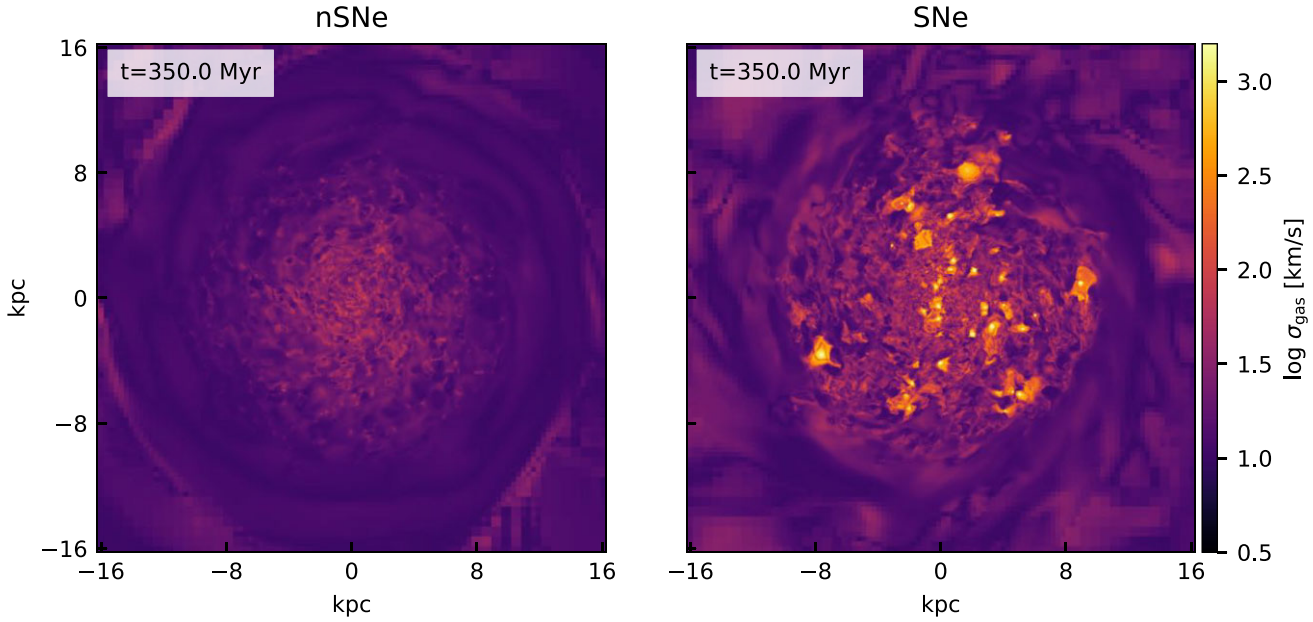

Figure 4. Line-of-sight gas velocity dispersion maps (in km s^{-1}) of the *nSNe* and *SNe* simulation at $t = 350$ Myr. The map scale is as in Fig. 1. For each plotted pixel, we calculated the velocity dispersion within a beam of ± 100 pc measured from the mid-plane. The width of the pixels are taken to be $\mathrm{d}x = 10$ pc. Recent SNe clearly increase the velocity dispersion within the low-density gas of the galaxy, indicating that the multiphase structure within the disc is not only driven by gravity and shear but also stellar feedback events.

simulation makes it apparent that the hot gas fills most of the galaxy volume, followed by the warm and then cold gas. For the *nSNe* simulation more volume is filled by the warm than hot gas (see Section 4.3 for a more quantitative discussion of the volume filling fractions, VFFs).

Fig.4 shows the vertical gas velocity dispersion for the *nSNe* and *SNe* simulation at a fixed time, $t = 350$ Myr. We measure the line-of-sight velocity dispersion map of the gas by projecting the galaxy face-on and include for each pixel of the image cells within a beam of ± 100 pc measured from the mid-plane of the disc. The width of the pixel and beam is taken to be $\mathrm{d}x = 10$ pc. For each beam, the line-of-sight gas velocity dispersion is calculated as

$$\sigma_{\mathrm{gas}} = \sqrt{\frac{\sum_i (v_{z,i} - \overline{v}_z)^2}{N}}, \tag{7}$$

where $v_{z,i}$ is the line-of-sight velocity in pixel i, $\overline{v}_z$ is the mean velocity within the beam, and N is the number of pixels in each beam.

The velocity dispersion within the galaxy in the *SNe* simulation is clearly higher than for the *nSNe* simulation. The very high velocity dispersion regions correlate with the low-density and hot temperature cavities carved by recent SN events, but the velocity dispersion also seems to be higher in regions of higher densities and lower temperatures.

In conclusion, we have seen that with SN feedback the ISM becomes multiphase and cavities are formed from the explosions that are low density and hot. The velocity dispersion is not only high within the cavities but also in warm gas. This indicates that the multiphase structure within the galaxy is not only driven by gravity and shear but also stellar feedback events. The ISM properties are further quantified in Section 4.3. The analysis of the kinetic energy power spectrum in Section 4.4 will additionally show that SNe feedback is important for the energetics of the ISM, especially for the warm phase that is only turbulent when SNe are included.

4.2 Star formation rates and the Kennicutt–Schimdt relation

The regulation of star formation is an essential aspect of any galactic star formation and feedback model and a probe of the efficiency of the feedback process. Without stellar feedback most of the gas within the galaxy would just be consumed and form stars. Star formation would then occur at a much higher rate and on shorter time-scales than observed. In this Section, we will investigate the ability of the SATIN model to regulate star formation. We look at different regions within the disc, probe different gas surface densities, and explore whether the SN explosions manage to regulate star formation in these regions. We will discuss which regions of the galaxy reach a self-regulated steady state due to SNe feedback. To call a region within a galaxy self-regulated we specifically require the surface density of the star formation rate ($\Sigma_{\rm SFR}$), the projected density of the gas ($\Sigma_{\rm gas}$), as well as the VFFs and mass filling fractions (MFFs) to remain constant over a certain time period (for a detailed discussion on the last requirements see Section 4.3). We then observe how well the measured $\Sigma_{\rm SFR}$ and $\Sigma_{\rm gas}$ match the KS relation and compare to observational data.

Fig.5 shows the total star formation history of the two simulated galaxies (*nSNe* and *SNe*). The blue bars show the instantaneous star formation rate for the *SNe* simulation computed as the sum of the star formation rates of each individual stellar cluster found within the galaxy at a given time t

$$\mathrm{SFR}_{inst} = \sum_{j=1}^{N_{sink}} \dot{M}_{sink,j}\,(\Delta t) \quad [\mathrm{M_\odot yr^{-1}}], \tag{8}$$

for $t - (\Delta t/2) < t < t + (\Delta t/2)$. We took a bin size of $\Delta t = 1$ Myr to calculate the instantaneous SFR. This corresponds to ∼2700 time-steps in the *SNe* simulation (the typical time-step is 370 yr).

The orange and dashed-pink line is an estimate of the observable SFR within the *SNe* and *nSNe* simulations. The plotted observable SFR takes into account the respective lifetime, $t_{\rm OB}$, of each individual massive star formed within the simulated stellar clusters. It therefore tries to mimic the SFR an observer would measure when tracing the SFR with Hα emission, where the emission sensitively depends on the presence of OB and WR-stars, something that we track directly in our simulations. The observable SFR is defined as

$$\mathrm{SFR_{OB}} = \sum_{i=1}^{N_\star} \frac{120}{t_{\rm OB,i}} \quad [\mathrm{M_\odot yr^{-1}}], \tag{9}$$

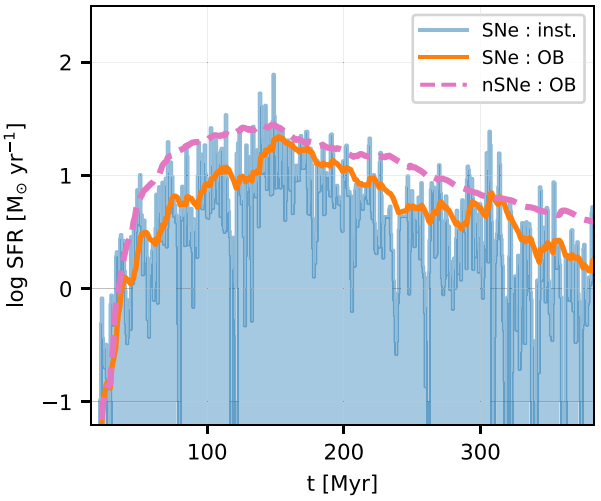

Figure 5. Global SFR history for the MW-like galaxy. The light-blue bins represent the instantaneous star formation rate for the *SNe* simulation computed as the sum of the individual instantaneous star formation rates of each individual stellar cluster at a given time t (see equation 8). The orange line shows the observed SFR values of the *SNe* simulation derived from the O- and B type star formation lifetimes (see equation 9). The dashed pink line shows the observed SFR values for the *nSNe* simulation. The SFR of the *nSNe* simulation is smoother and higher by a factor of 2 (as a mean value for the length of the simulation) than the SFR of the *SNe* simulation. SFR in both simulations decreases with time after 100 Myr but the SFR is much more stochastic for the *SNe* simulation.

where $t_{\mathrm{form},\,i} < t < t_{\mathrm{form},\,i} + t_{\mathrm{OB,\,i}}$. Here $t_{\mathrm{form},\,i}$ is the time of formation of massive star i, and $N_\star$ is the total number of massive stars at time t (taken from Gatto et al. 2015).

For the first 150 Myr, the total SFR of the *SNe* simulation rises steadily due to the fragmentation of the initial gaseous disc and the subsequent formation of stars within the galaxy. At this stage, the galaxy has consumed only about 5 per cent of the total gas mass present at the beginning of the simulation. Following this 'star-burst' phase, the SFR decreases for the rest of the simulation. This is due to three important aspects: first, the rapid formation of stars at the beginning of the simulation quickly removes dense gas around the star clusters. Secondly, the SNe additionally increase the turbulence within the gas in the galaxy. Thirdly, the SNe manage to push out gas from the galaxy. All of this leads to a decline in gas accretion onto the star clusters and results in a reduction of the newly formed stars. Towards the end of the simulation, the total SFR of the *SNe* simulation approaches 3 $\mathrm{M_\odot\ yr^{-1}}$, which is within the range of uncertainties of SFR measurements of this galaxy type (Kennicutt & Evans 2012; González Delgado et al. 2017; Zhou et al. 2023). However, given that its SFR is still decreasing at the end of the simulation, we note that the whole galaxy has not (yet) reached a completely self-regulated steady state.

The *nSNe* (dashed pink) and *SNe* (orange) simulations only start to differ after the first SNe explode around 22 Myr, where the SFR rises more steeply for the *nSNe* until around 150 Myr. However, the *nSNe* galaxy consumed at this stage already 30 per cent of the original total gas mass within the galaxy, compared to 5 per cent for the *SNe* simulation. This shows that the SNe reduce the accretion of gas onto the star cluster already in the star-burst phase and subsequently lower the rate at which stars are formed early on. After this first rise, the SFR of the *nSNe* declines steadily until the end of the simulation, continuously consuming gas. The constant disruption of

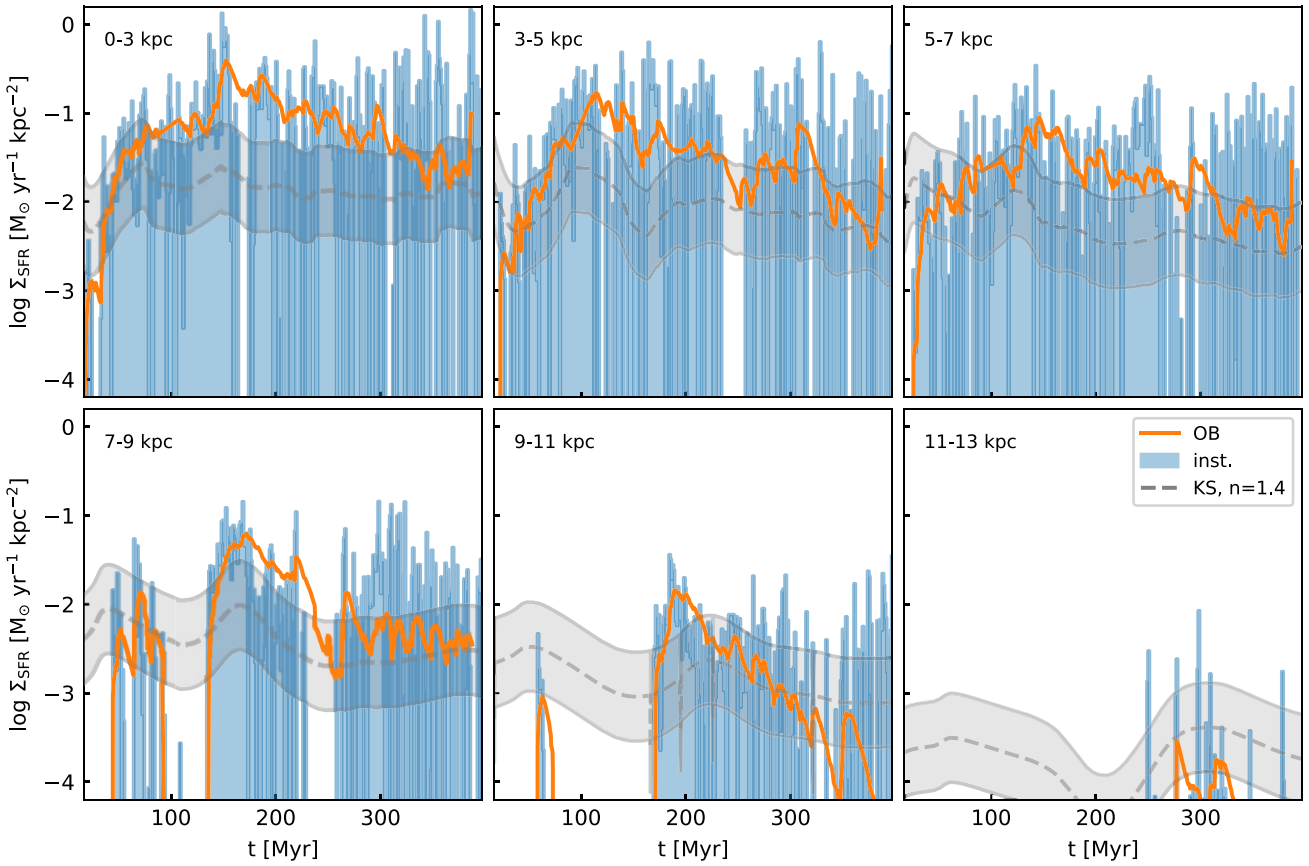

Figure 6. Evolution of $\Sigma_{\rm SFR}$ within different concentric cylindrical rings (radius range written in figure panel). Blue is for $\Sigma_{\rm SFR\ inst}$, and the orange line for $\Sigma_{\rm SFR\ OB}$ for the *SNe* simulation, respectively (as in Fig. 5). The grey dashed line represents the expected $\Sigma_{\rm SFR}$ from the KS relation for the calculated surface density within the cylindrical ring at a given time. The grey band indicates a factor of two uncertainty. For a visual impression of the different radii within the gas density distribution at t = 350 Myr, see Fig. 2. SN feedback alone regulates SFR well in lower surface density environments (i.e. radii at and above solar neighbourhood around 7–9 kpc). For higher surface densities, SNe alone is, at early times, not sufficiently limiting SFR. Early feedback from radiation, cosmic rays, and stellar winds likely would help.

the gas distribution around the star clusters manifests in much more SFR variation on short timescales compared to the *nSNe* simulation.

Turning on SN feedback reduces the formation of stars by a factor of two as a mean value over the duration of the simulation (see also Fig. B1 for the evolution of the total mass of newly formed stars). After 400 Myr, the *nSNe* simulation consumed more than 80 per cent of the initial gas mass within the galaxy and turned it into stars. On the other hand, the *SNe* simulation only consumed 42 per cent of the gas mass due to the presence of the SNe feedback.[5] SNe feedback induces turbulence within the gas as well as pushes gas outside the galaxy, both reducing gas accretion onto the star clusters and the formation of stars within them. Part of the ejected gas is recycled and used to sustain star formation at later times.

As the global SFR is still decreasing at the end of the simulation we conclude that the galaxy has not (yet) reached a self-regulated state. We will now look at different regions within the galaxy and probe the capability of SNe feedback to regulate SF in different gas surface densities environments. For this, we will analyse the KS relation (Kennicutt 1998a) that connects the projected density of the gas ($\Sigma_{\rm gas}$) to the surface density of the star formation rate ($\Sigma_{\rm SFR}$). Recall that our requirement to call a region within a galaxy self-regulated is that $\Sigma_{\rm SFR}$, $\Sigma_{\rm gas}$, as well as the VFFs and MFFs remain constant over a certain time period (for a detailed discussion on the last requirements, see Section 4.3).

Fig.6 shows the SFR surface density within different rings in the galaxy as a function of time. Similar to Fig. 5, the blue bars show the instantaneous star formation rate surface density and the orange line shows the observable SFR surface density evolution defined in equation (9) within the indicated rings. A visual guide of the ring boundaries is shown in Fig. 2. Overplotted in a grey dotted line is the calculated $\Sigma_{\rm SFR}$ assuming that it follows the universal KS relation, $\Sigma_{\rm SFR} \propto {\Sigma_{\rm gas}}^{1.4}$, where $\Sigma_{\rm gas}$ is the measured gas surface density at the given time. We calculated $\Sigma_{\rm gas}$ taking into account all gas between $z = \pm 250$ pc and within the respective ring boundaries centred on the galaxy.[6] The grey band shows an observational uncertainty of 1 dex around $\Sigma_{\rm SFR}$ (t).

After ~300 Myr, the measured $\Sigma_{\rm SFR}$ lie within the observational uncertainties for star-forming galaxies in all rings. For higher gas surface densities or within the inner 7 kpc in the disc, the SFR surface density is at the upper end of the margin or more in the star-bursty regime (see also Fig. 7 and discussion below). The SFR surface densities are, for rings within 7 kpc, still declining at the end of the simulation, whereas the gas surface densities (indirectly shown

[5]This means that ~2 per cent of the gas leaves the galaxy.

[6]We tested that by using a larger delta z we do not change the results significantly as there is not much mass above these distances.

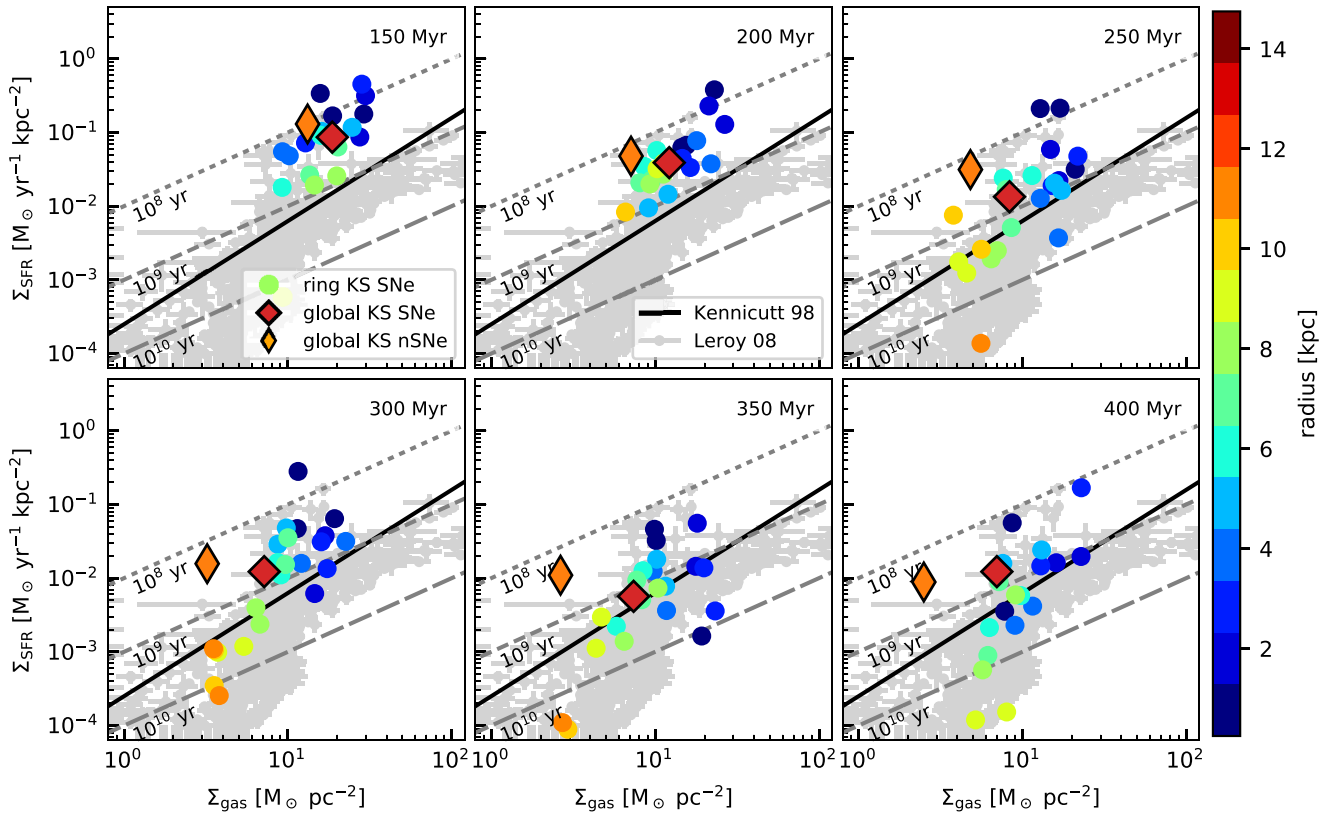

Figure 7. KS Relation for different rings (indicated by different colours) within the galaxy at a given time. The global KS for the *nSNe*/*SNe*simulation is calculated within a fixed radius of $r = 8$ kpc. The solid black line is the KS relation. The different dotted lines show constant depletion times of 10, 1, and 0.1 Gyr from the bottom to top. We compare the simulated values to observational data of Leroy et al. (2008). Our *SNe* simulation compares well with the observational sample. The rings as well as the global value start within the star-bursty regime above the KS value and move closer around the KS relation with time. SNe regulate SFR early for low surface density regions, whereas for higher surface densities (above solar neighbourhood) it takes a little bit longer, potentially because SNe do not act fast enough. Without SNe, the global KS value stays well within the star-burst regime and/or outside observational values.

via the grey dotted line) remains fairly constant after ∼250 Myr. In other words, we see that these high-density regions have, in our simulations, not (yet) reached a self-regulated state. However, for gas surface densities close to the radius of our solar neighbourhood (between 7 and 9 kpc from the centre of the galaxy) we find that Σ_{SFR} lies well within the KS relation after around ∼250 Myr of simulation time. The equivalent Σ_{SFR} of the *nSNe* simulation is, at the same time, well above the KS relation and continuously decreasing. After ∼250 Myr, the gas and SFR surface densities, as well as the VFFs and MFFs (see Section 4.3) stay, for the *SNe* simulation, constant over time. Given our definition for self-regulation, we conclude that this region of the galaxy is due to the presence of SNe self-regulated. This is very likely due to the lower environmental hydrogen density that then causes the SNe to be efficient in driving a wind. We will explore this in more detail in future work. Finally, for lower Σ_{gas} at radii larger than 9 kpc, the SFR surface density lies below the KS but still within the observational uncertainty plotted. At the same time, both Σ_{SFR} and Σ_{gas} are still declining. As already seen in Fig. 3, the gas structure outside ∼9 pc is at the end of the simulation still very smooth and cold. It is therefore not surprising that this region has not yet reached a self-regulated state.

Fig.7 shows the relation between SFR and gas surface densities for different rings (indicated by different colours) within the galaxy at different times. We also show the global KS for the *nSNe*/*SNe* simulation computed from the total SFR rate and the total gas mass within $r = 8$ kpc. To guide the eye we also plotted the KS relation (Kennicutt 1998b) as a solid black line. The different dotted lines show constant depletion times of 10, 1, and 0.1 Gyr from bottom to top. The obtained simulation relations are compared to the observational data of Leroy et al. (2008) that also show significant scatter around the KS value.

Similar to the findings from Fig. 6, we find that all the rings, as well as the global KS values, lie within the observational sample shown. At the beginning of the simulation ($t < 250$ Myr) Σ_{SFR} lies, for the rings as well as the global value, above the KS relation and thus within the star-bursty regime. Around $t = 250$ Myr, the simulation scatters close but mostly above the KS relation. The rings with higher surface densities or, in other words, the rings closer to the centre of the galaxy lie more within the star burst region of the KS relation and approach the KS relation only around 300 Myr. The rings with lower surface densities are already early on close to the KS relation. The global KS value for the *SNe* simulation shows that gas is converted into stars on a typical time scale of 0.5–2 Gyr, which is much longer than the free fall time of the star forming gas, with $\rho_{sink} = 50$ H cm^{-3} and $t_{ff} \sim 7$ Myr. The resulting star formation rate in our simulation is thus rather inefficient. Without SNe regulation the global value stays well within the star-burst regime and/or outside observational value. This is in agreement with the discussion above.

To conclude, we find that in our simulations SNe are efficient enough to bring the SFR within observational uncertainties and around the KS value for solar neighbourhood-like surface densities. Within the solar neightborhood, the galaxy reached a self-regulated

steady state. This is not the case for the outskirts of the galaxy (radii larger than 9 kpc) where the gas has not yet collapsed and is still smooth. For larger surface densities, the SFR surface densities are more in the star-bursty regime, but approach the KS relation. Additionally, these higher density regions never reach a self-regulated steady-state state as $\Sigma_{\rm SFR}$ still keeps decreasing at the end of the simulation. Early feedback by, for instance, radiation from the stars or stellar winds might help to limit SFR as it prevents gas from accreting onto the stellar clusters (Bieri et. al. in preparation).

4.3 Multiphase ISM structure

Capturing a turbulent multiphase ISM is an important goal of the SATIN simulation project. To analyse the properties of the ISM structure we define three different gas phases in our simulation: The cold ($T < 300$ K), warm ($300\ {\rm K} \leq T < 2 \times 10^4$ K), and hot ($T \geq 2 \times 10^4$ K) medium. The properties of these phases is regulated by a complex interplay between cooling, self-gravity, turbulence, shear, and heating from SNe feedback during the evolution of the galaxy. In this Section we show that with SNe feedback included the gas within the galaxy is multiphase, the phase diagram populates larger regions that are thermally unstable, and that after some time the VFFs as well as MFFs stay remarkably stable within 7 kpc.

Fig.8 shows the phase diagram of all the gas cells within a cylindrical region of $r \leq 10$ kpc and $z \leq \pm 250$ pc, averaged over the time period of ± 10 Myr around 350 Myr. The two-dimensional temperature versus density histogram is additionally coloured by the total mass within the pixel. We highlight the temperature cuts for the different gas phases in blue (i.e. temperature cut for cold gas) and red (i.e. temperature cut for hot gas).

For both *SNe* and *nSNe* simulations, the density covers several orders of magnitude in the range from $\sim 5 \times 10^{-5}$ to $\sim 5 \times 10^2$ H cm^{-3}. In both simulations, a large fraction of the warm gas is close to the equilibrium cooling curve. Due to SNe feedback, however, a lot more gas populates regions in the phase diagram that are thermally unstable as the explosions disrupt the gas and eject hot gas from within the star forming disc. As a result, the hot gas covers a larger density range for the *SNe* simulation. The cool gas reaches densities of $\sim 10^{-1}$ H cm^{-3} as only gas that is dense enough can effectively self-shield from the UV background, cool down, and eventually become dense enough to form stars. The colouration of the phase diagram indicates that the cold, high-density gas makes up most of the mass within the galaxy.

We highlight the gas that is above the sink formation threshold (i.e. $\rho_{\rm sink} = 50$ H cm^{-3}). Star clusters can only form from gas with this density and higher, but only after it will collapse gravitationally (see Section 2.3). For the *SNe* simulation, there is a substantial amount of colder (below 10 K) high-density gas above the sink formation threshold. This is because the SNe disrupt the high-density gas more and as a result fewer high-density gas clumps fulfill the requirements for sink formation/accretion. The fraction of gas that remains is influenced by the formation/accretion criteria. In future work, we will study in more detail how changing the requirement for formation/accretion will change gas distribution of the different gas phases. It is possible that having a less strict requirement such as Kim & Ostriker 2018; Moon et al. 2021 might reduce the amount of gas that remains cold within the galaxy. In addition, we also possibly miss important physical processes such as cosmic rays, ionization, and winds from the stars. Those effects could likely prevent the formation of the coldest gas in this diagram (see also Peters et al. 2015; Geen et al. 2015b; Girichidis et al. 2016; Simpson et al. 2016; Gatto et al. 2017; Peters et al. 2017). We plan a more detailed investigation in future work.

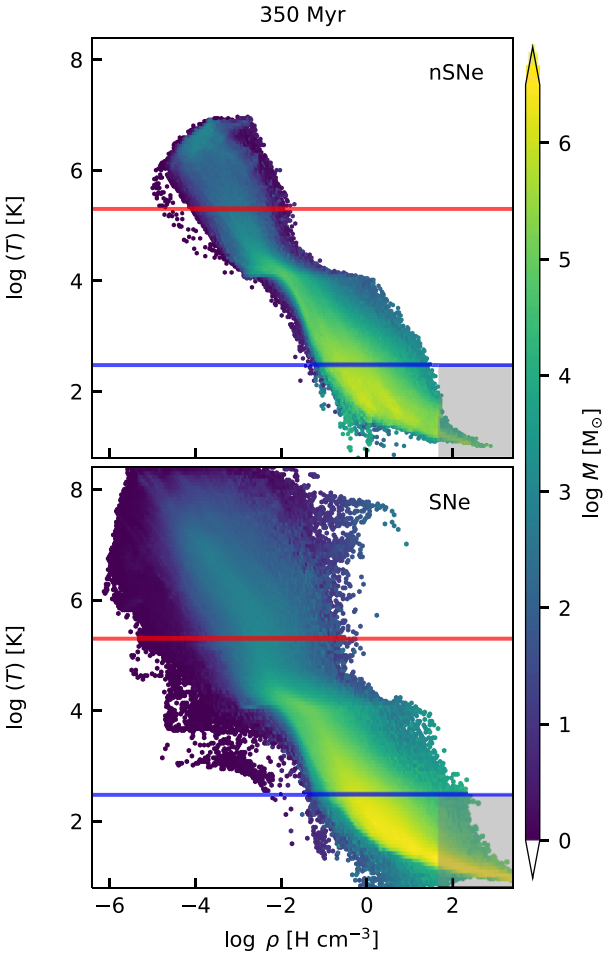

Figure 8. Two-dimensional temperature versus density diagram of all the gas cells within a cylindrical region of $r \leq 10$ kpc and $z \leq \pm 250$ pc. We average the phase diagram over the time period of ± 10 Myr around 350 Myr. The diagram is coloured by the total mass within the pixel. The lines highlight the temperature cuts for the different gas phases in blue (cut for cold/warm gas) and red (cut for warm/hot phase). We additionally highlight the gas that is above the sink formation threshold (i.e. $\rho_{\rm sink} = 50$ H cm^{-3}). Due to the SNe feedback, a lot more gas populates regions that are thermally unstable because the explosions disrupt the gas and eject hot gas from within the star forming disc. The gas within the *SNe* simulation reaches both lower and higher densities.

We identify the gas volume and mass in the different phases within cylindrical rings (radii indicated in the axis label) and $z \leq \pm 250$ pc for different times (150–400 Myr in 50-Myr spacing) in Fig. 9. Generally, after 150 Myr the hot gas fills most of the volume (~50 per cent), followed by the warm (~30–35 per cent) and then cold phase (~15–20 per cent). The VFFs in the central region ($r < 7$ kpc) stay remarkably stable with time. Around the solar neighbourhood ($r = 7$–9 kpc) the VFF oscillates more. However, once the SFR surface density reaches the KS value for these gas surface densities at around 300 Myr (see Fig. 6), the VFF also shows less variation over time. For regions further out in the galaxy ($r > 9$ kpc), where stars start to form much later and the density region is still very smooth and cold at the end of the simulation time, the VFF continues to vary for the duration of our simulation.

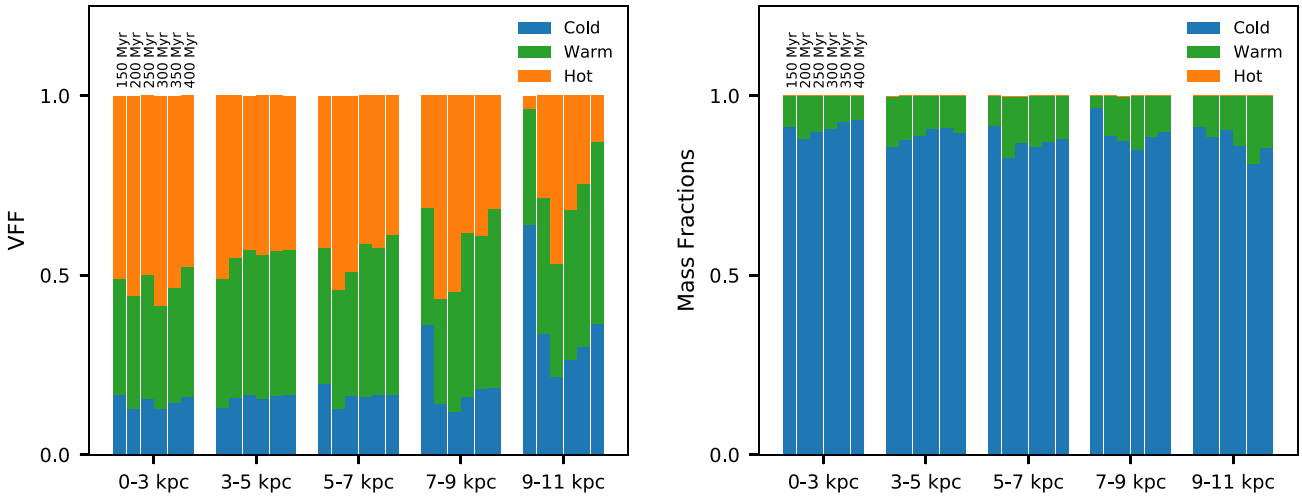

Figure 9. VFFs and MFFs for different times (150–400 Myr in 50-Myr spacing) and different cylindrical rings (radii indicated in the axis label) for the *SNe* simulation at the top/bottom panel. For the *SNe* simulation, the hot gas fills most of the volume (∼50 per cent), followed by the warm (∼30–35 per cent), and then cold phase (∼15–20 per cent). Once the SFR surface density reaches KS value for the corresponding surface densities the VFF is stable with time, except for the regions further out in the galaxy ($r > 9$ kpc). The high-density cold gas makes up most of the mass in the galaxy (∼85–90 per cent), followed by lower density, warm gas (∼10–15 per cent) produced mostly through SN heating. The hot phase only makes up to 0.5 per cent. Comparing to models for the ISM phase based on observations we underestimate/overestimate the VFF in the warm/hot phase. Early feedback by radiation that disrupts the dense gas in star-forming regions and thus increases/decreases the VFF in the warm/hot phase would likely help.

As already noted above, cold, high-density gas makes up most of the mass in the galaxy's disc (∼85–90 per cent), followed by lower density, warm gas (∼10–15 per cent) produced mostly through SN heating. The hot phase only makes up to 0.5 per cent. For regions within 9 kpc, the MFFs stay, after ∼250 Myr, stable with time, whereas it keeps varying for the outer region of the disc.

This solidifies our findings (see Section 4.2) that within the solar neighbourhood, the galaxy reached, after 300 Myr, a self-regulated state.[7] Larger surface density regions (radii smaller than 7 kpc) have, due to $\Sigma_{\rm SFR}$ still decreasing, not (yet) reached a self-regulated state although $\Sigma_{\rm gas}$, VFF, and MFF stay remarkably constant over time. This is because most of the gas is in this region in the dense cold star forming clouds where SNe feedback slightly disrupt, but not destroy, the clumps such that the gas does not fulfill the requirement for sink formation/accretion. The outskirts of the galaxy also have not reached self-regulation as the gas within this region has not yet formed a stable multiphase structure causing the VFFs, MFFs, as well as $\Sigma_{\rm SFR}$ and $\Sigma_{\rm gas}$ to not be constant with time.

The same analysis for the *nSNe* simulation (not shown) reveals that the inner region shows a similar behaviour as for the *SNe* simulation. This indicates that SNe is insufficient to regulate star formation in the central dense region of the galaxy and that the evolution of this inner region is driven by rotation and shear. The intermediate regions ($r =$ 3–9 kpc) have, for the *nSNe* simulation, not reached a steady state as the mass and VFFs for the cold phase keeps decreasing for the length of the simulation due to the ever accreting sinks. The outskirts of the galaxy equally has not reached a steady-state for similar reasons as for the *SNe* simulation. The *nSNe* simulation has most of the mass in the cold phase and close to no mass in the hot phase.[8]

As we will discuss in more detail in Section 5 compared to observations the SATIN1 *SNe* simulation matches the VFF of the cold phase range, but slightly underestimate/overestimate the VFF in the warm/hot phase. In addition, we underestimate/overestimate the MFF of the warm/cold gas in the solar neighbourhood (see e.g. McKee, Parravano & Hollenbach 2015). Peters et al. (2017) reported similar results for their SNe only simulation and showed that only their simulation including radiation from the stars approached observed values. This early pre-SN feedback via energetic radiation of massive stars disrupts the dense gas in star-forming regions and by doing so increases/decreases the VFF in the warm/hot phase. Simultaneously, this also may help to self-regulate SFR in the central region.

The differential gas mass (top panel) and volume (bottom panel) distribution displays each gas phase in the ISM in another way. Fig. 10 shows the distributions for the *nSNe*/*SNe* simulation at 350 Myr averaged over ±10 Myr. To calculate them we only take the gas within the disc using a spatial cut of $r = 10$ kpc and $z \leq \pm 250$ pc (as for the phase diagram above).[9] The different colours in the figure highlight the contributions of the cold (blue), warm (orange), and hot (red) to the total (black) gas within the ISM. As a consequence of the SNe feedback, the galaxy shows a clear bimodal character in the total volume and a hint of a bimodal character in the mass distribution. This multiphase ISM character, especially the prominent low-density peak, is less apparent for the *nSNe* simulation.

The warm and cold dominated phases transition at similar densities (∼100 H cm^{-3}) for both the *nSNe* and *SNe* simulation. At higher densities cold gas dominates in both distributions. The gas within the *SNe* simulation reaches both lower and higher densities compared to the *nSNe* simulation. The injected kinetic energy due to the SNe explosions prevents some of the cold gas from accreting onto the sink leading to the observed higher densities. Additionally, the SNe

[7]Recall that our requirement to call a region within a galaxy self-regulated is that $\Sigma_{\rm SFR}$, $\Sigma_{\rm gas}$, as well as the VFFs and MFFs remain constant over a certain time period.

[8]The *nSNe* simulation has no process to create hot gas after the two initialization stages. All of the hot gas comes from the SNe in the initial turbulence injetion phase (see Section 3.1).

[9]We tested several different radii and height cutoff values to confirm that the qualitative result does not change.

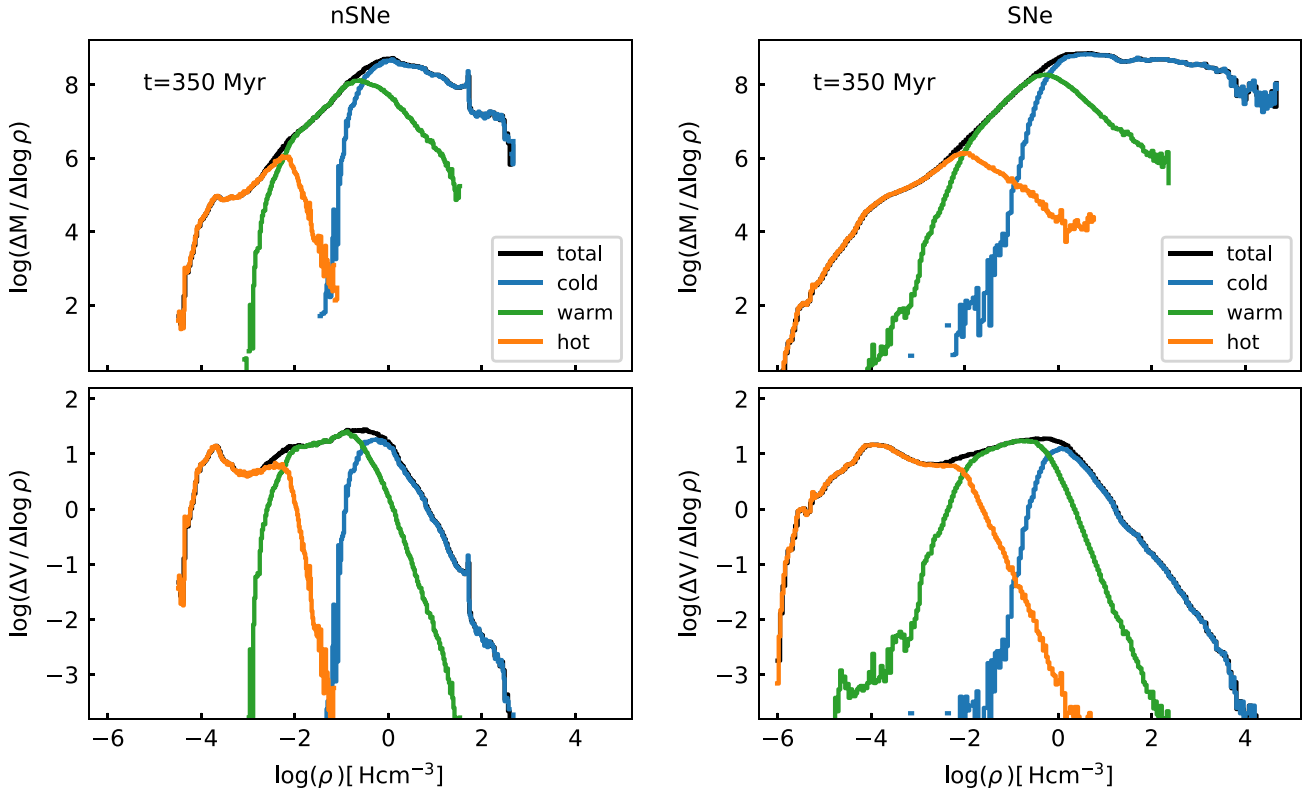

Figure 10. Differential gas mass (top panel) and volume (bottom panel) distribution as a function of the gas density at time $t = 350 \pm 10$ Myr for the simulated *nSNe*/*SNe* galaxies. We only take gas within a cylindrical region of $r = 10$ kpc and $z \leq \pm 250$ pc. The distributions are shown for all gas (black), as well as the cold (blue), warm (orange), and hot (red) gas phase within the ISM. As a consequence of SNe feedback, a multiphase structure forms in the ISM. This leads to a clear bimodal character of the volume distributions and a hint of a bimodal character of the mass distribution for the *SNe* simulation. The gas within the *SNe* simulation reaches both lower and higher densities as SNe explosions halt the cold gas from further collapse, and heat and disperse the gas.

also heat and disperse the gas causing the distribution to have lower densities, and the hot phase to dominate to higher densities ($\sim 10^{1.8}$ H cm^{-3}) for the *SNe* simulation compared to the *nSNe* simulation ($\sim 10^{1.2}$ H cm^{-3}).

To summarise, the SATIN1 simulations capture a distinct multiphase ISM with three coexisting gas phases. With SNe included the gas populates larger regions in the phase diagram especially some that are thermally unstable. Because of the lack of SNe the ISM the *nSNe* is smoother and does not reach as low/high densities. As we will also show more in the next section, the creation of the multiphase ISM is, in our simulated galaxies, not only due to SNe feedback ut also cooling, gravity, and shear.

4.4 ISM turbulence

In this section, we will look more closely at the impact of SN feedback in shaping the energy structure of the ISM. The turbulent ISM can be quantified in Fourier space using power spectra, which is often used in the context of turbulent flows. On galactic scales, simulations (e.g. Wada, Meurer & Norman 2002; Agertz et al. 2015; Grisdale et al. 2017) and observations of the neutral ISM in nearby galaxies (e.g. Stanimirovic et al. 1999; Bournaud et al. 2010; Combes et al. 2012; Zhang, Hunter & Elmegreen 2012; Dutta & Bharadwaj 2013) show that turbulent scalings are present over several orders of magnitude in scale. It is, however, not yet fully established what physical mechanisms (gravity, shear, accretion, feedback) maintain the turbulence on these galactic scales. The interested reader may be referred to (Pfrommer et al. 2022) investigating in more detail different turbulence driving mechanisms in MW-like discs.

We calculate power spectra of the specific kinetic energy by taking the absolute square of the Fourier transform of $\sqrt{\rho}\mathbf{v}$ and dividing in the end the kinetic energy power spectra by the total gas mass within the box. The chosen uniform box is centred on the disc, has a physical extent of $r_{\rm box} \simeq 15$ kpc, is zero padded to $2 \times r_{\rm box}$, and has a uniform resolution of 40 pc. A more detailed description of the power spectra calculation can be found in Appendix C.

Fig.11 shows the kinetic energy power spectrum at $t = 350$ Myr averaged over ± 10 Myr. In the top and middle panel we show the different contributions of the cold (blue), warm (orange), and hot (red) phase to the total power spectrum (black) of the *nSNe* and *SNe* simulation. In the bottom panel the *SNe* over *nSNe* ratio of the power spectra is shown. The vertical line shows the wavenumber corresponding to a physical length of 420 pc ($\sim 46\Delta x$) and is where the power spectrum drops of steeply. We attribute the drop/break in the power spectrum to the scaleheight of the cold disc causing a transition from 2D turbulence on large scales to 3D turbulence on scales $l \lesssim h$. Broken power laws have also been studied in earlier work (see e.g. Elmegreen, Kim & Staveley-Smith 2001; Padoan et al. 2001; Dutta et al. 2009a; Zhang et al. 2012) and are also observed (see e.g. Dutta et al. 2009b; Combes et al. 2012).

The kinetic power spectra for the two simulations show that at large scales most of the kinetic energy is in the hot gas. The power-law behavior of the hot gas shows that it is also turbulent and thus most of the energy resides at the top of the self-similar cascade where turbulence is driven. Both *nSNe* and *SNe* simulations show a

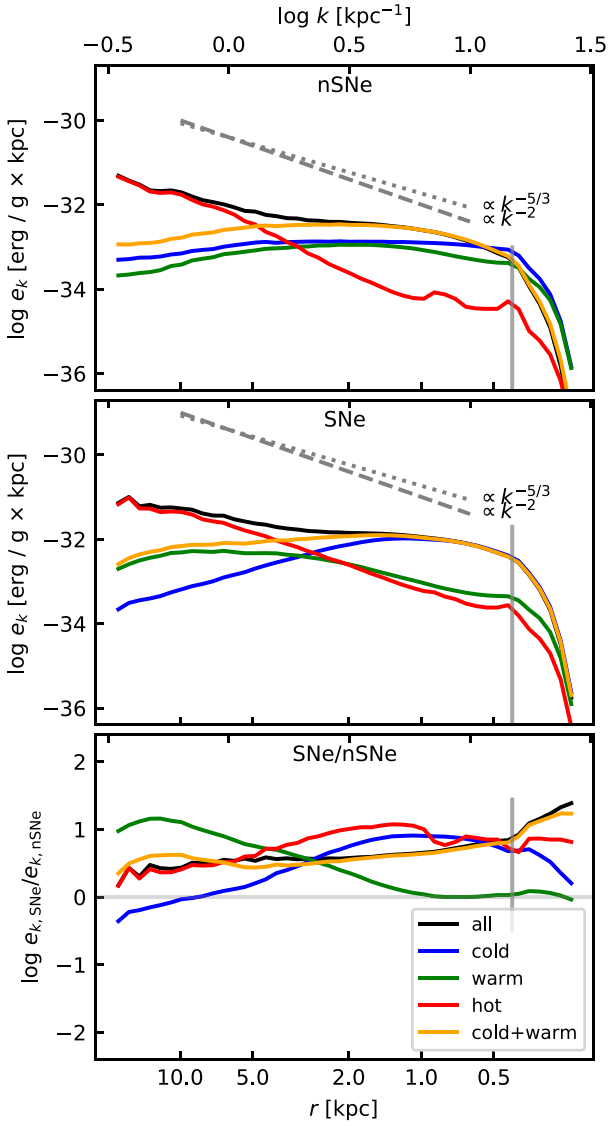

Figure 11. Specific kinetic energy power spectrum at $t = 350$ Myr averaged over ±10 Myr. The top/middle panel show the different contribution of the cold (blue), warm (orange), and hot (red) phase to the total power spectrum (black) of the *nSNe*/*SNe* simulations. The bottom panel shows the ratio of the specific kinetic energy power spectra of *SNe* over *nSNe*. The physical scale l is connected to the wave vector via $k = 2\pi/l$. The vertical line corresponds to a physical length of 420 pc ($\sim 46\Delta x$) and is also where the power spectra drop of steeply. The drop/break in the power spectrum is likely due to the finite thickness of the (cold) disc causing a transition from 2D turbulence on large scales to 3D turbulence on small scales. The power spectra of the *SNe* simulation have more specific kinetic energy at all scales for all gas phases. SNe feedback is thus an important driver of the density and energy structure of the ISM. For the hot gas, turbulence is driven by a combination of gravity, shear, and the initial SNe explosions. Continuous SNe explosions are, in addition, driving turbulence as only the power spectrum for the *SNe* shows super-sonic ($e_k \propto k^{-2}$, between 550 pc and 10 kpc) for the hot and Kolmogorov ($e_k \propto k^{-5/3}$, between 450 pc and 4 kpc) scaling for the warm gas.
Finally, the cold gas does not show any turbulent scaling as the SNe feedback does not manage to disrupt the cold and dense clouds within the galaxy.

power-law behavior in the hot phase that is driven by a combination cooling, gravity and shear, as well as the initial turbulence-driving SNe explosions (see also Pfrommer et al. 2022). However, only the *SNe* simulations shows scalings that are, between 550 pc and 10 kpc, in good agreement with that for for super-sonic turbulence (i.e. $e_k \propto k^{-2}$; Burgers 1948). This supports that the SNe explosions are in our simulations, in addition, driving turbulence.

At 4 kpc the total power spectra transitions into a shallower relation and the kinetic energy of both the cold and warm gas together start to dominate. We find that only the slope of the warm gas for the *SNe* simulation follows that for subsonic Kolmogorov turbulence ($e_k \propto k^{-5/3}$, between 450 pc and 4 kpc; Kolmogorov 1991). The cool gas is not turbulent in both *nSNe* and *SNe* simulations because the corresponding power spectrum does not show a power-law behaviour. The cool gas is, however, still important for the energetics of the ISM, especially in the *SNe* simulation, on scales smaller than 3 kpc. It seems that for the cold gas, large scale turbulence (i.e. large scale rotation and gravitational instabilities) is no longer present, as most of the power is now 'locked-up' in the dense cold star forming clouds instead of being disrupted and returned back to the large scale driving. This is because the dense star forming clouds are only slightly disrupted, but not destroyed, by the SNe explosions. For all gas phases and both simulations the power spectrum drops off steeply below 420 pc ($\sim 46\Delta x$), likely due to the finite thickness of the (cold) disc causing a transition from 2D turbulence to 3D turbulence on small scales. The ratio of the power spectra for the two simulations shows that the *SNe* simulation has more kinetic energy at all scales and for all gas phases. This shows again that SNe increase the kinetic energy of the cold gas that is cooling out of the warm phase. We also find that feedback regulation results in steeper power spectra for the warm gas (similar results have been found by Grisdale et al. 2017). We find the same quantitative result for the kinetic energy power spectra.

To conclude, by looking at the power spectrum we find that SN feedback is an important driver of the density and energy structure of the ISM (up to ∼12 kpc) and that it helps to shape the power spectra, especially for the warm gas phase. However, the comparison between the *SNe* and *nSNe* simulations shows that cooling, gravity, shear, and accretion also contribute significantly to the specific kinetic energy at all scales and are therefore also important for the energetic structure of the ISM. In our simulations most of the power in the cold phase is in the star forming clouds as SN feedback does not manage to fully disrupt the dense clumps and to drive turbulence on galactic scales for the cold gas. The effect of early stellar feedback by radiation and winds as well as cosmic ray heating would prevent the formation of the coldest gas within the galaxy and thus would change the energetics of the ISM. We leave the detailed investigation of the missing physical mechanisms and their effect on the ISM and power spectrum to future work.

4.5 Gas dynamics and flows

Gas flows in and out of galaxies are important in regulating star formation as well as to drive turbulence within the galaxy. In this Section we will discuss that the SNe generate multiphase gaseous outflows. The cold and warm gas is recycled and builds a fountain flow sustaining the formation of stars. Later the SNe push the hot gas far enough from the galaxy such that it does not fall back. We will only discuss the *SNe* simulation in this Section as the *nSNe* simulation does not create any outflow.

Fig.12 shows the measured gas outflow rate (OFR; top left-hand panel), inflow rate (IFR; top right-hand panel), mass loading (η = OFR/SFR; bottom left-hand panel), as well as the ratio of the

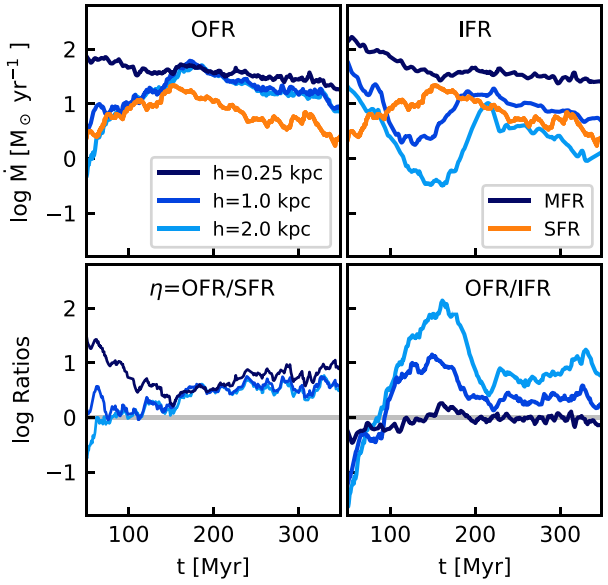

Figure 12. Total outflow rate (OFR; top panel) and inflow rate (IFR; middle panel) as a function of time; calculated at different heights and compared against the total SFR. The bottom panel shows the mass loading (η = OFR/SFR) as well as OFR/IFR. The mass flux is calculated at r = 13 kpc and within a slab at different heights ($h = \pm 0.25, \pm 1, \pm 2$ kpc). The IFR close to the disc follows closely the OFR at the same height. The ratio of OFR/IFR is above unity the further away from the galaxy. After 200 Myr, the mass loading factor evolves around the same value ($\eta \sim 5$) for $h > 0.25$ kpc and a slightly higher value ($\eta \sim 7$) for $h = 0.25$ kpc. After 200 Myr, the SNe explosions are, therefore, efficiently pushing the gas far away from the galaxy.

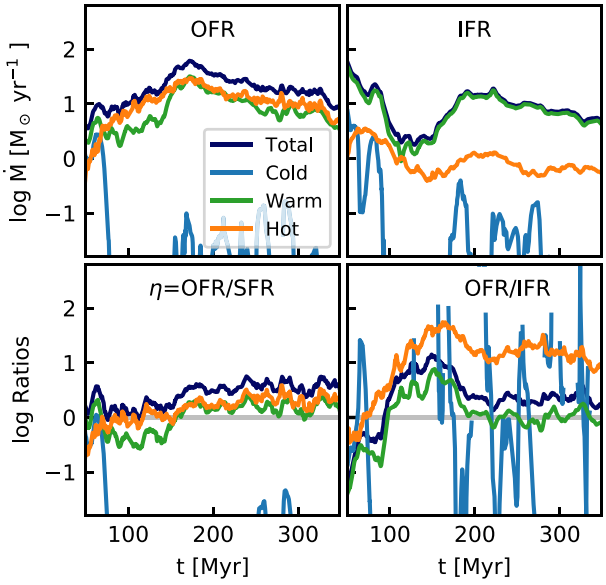

Figure 13. OFR/IFR as a function of time for the different phases in the top panel, both also compared against the total SFR. Mass loading (η = OFR/SFR) and OFR/IFR for different phases is shown in the bottom panel. The mass flux is calculated at $r = 13$ kpc and within a slab at $h = 1$ kpc. After ~150 Myr, the warm gas that is pushed out by the SNe has the highest contribution to the total mass outflow/inflow rate. The hot gas contributes little to the total OFR. However, most of the gas that leaves the galaxy is hot as it has the highest OFR over IFR ratio. The warm gas builds a fountain flow and falls back onto the galaxy fueling star formation.

OFR over IFR (bottom right-hand panel); all measured at different heights above and below the mid-plane of the galaxy ($h = \pm 0.25$, ± 1, ± 2 kpc) and also indicated in the legend. Overplotted is the total SFR within the galaxy for comparison (top/middle panel).

To compute the mass flux, we only consider gas at a radius of $r \leq 13$ kpc and within a slab at different heights above and below the mid-plane of the galaxy.[10] The gas mass flux is then calculated as

$$\dot{M}_{\rm gas} = \oiint_{\rm slab} \boldsymbol{v} \cdot \hat{\boldsymbol{r}} \, {\rm d}S = \sum_{i \in {\rm slab}} m_i \, \boldsymbol{v}_{z,i} \, / \Delta z, \tag{10}$$

where i denotes the index of a cell within the slab at height $\pm h$ measured from the mid-plane of the galaxy. We adopt a slab thickness of $\Delta z = 500$ pc. Positive/negative velocities v_z with respect to the disc plane contribute to the outflow/inflow.

Until the SFR declines around 200 Myr the OFR is highest closer to the galaxy and then progressively decreases further away from the galaxy. Afterwards the OFR settles around 30 $M_\odot$ yr^{-1} at all heights, with only a slow decline over time. This is half an order of magnitude higher than the measured total SFR within the galaxy, also shown in the mass loading factor ($\eta \approx$ 3–10) in the bottom panel. The OFR, calculated at $|h| \geq 1$ kpc, noticeable follows, with a short delay, the SFR. After 200 Myr the mass loading factor settles at the same value for all heights greater than ± 0.25 kpc away from the galaxy to $\eta \approx 5$. This indicates that, after some time, the outflow is directly correlated with the SFR. But not only the global OFR is correlated with the SFR, as similar outflow measurements for different radii within the disc also have shown that the OFR is strongest near the galactic centre, where star formation is most effective.

The IFR decreases for the first 150 Myr and more drastically the further away in height from the galaxy. This is most likely due to adiabatic contraction and further settling of the initial conditions. With the increasing SFR the IFR also starts to increase with a short time delay at distances above 1 kpc. Once the SFR decreases, around 200 Myr, the IFR also starts to decrease, again with a short time delay that is longer at larger distance away from the galaxy. The highest IFR is closest to the disc and one measures progressively lower rates the further out vertically from the galaxy. The IFR close to the disc follows closely the OFR calculated at the same height; also shown by the very close to unity ratio of the OFR over IFR shown in the bottom right-hand panel. The OFR/IFR ratio is further above unity at larger galactic heights. Measurements at $h = 20$ and 30 kpc show that the mass loading at these distances have a mass loading of $\eta \approx$ 1 and 0.1, respectively. The mass loading is also at these distances constant and does not drop significantly with time. This shows that some of the gas that is pushed away from the galaxy likely does not fall back.

The mass loading of the *nSNe* simulation (not shown) changes from $\eta = 0.7$ to 0.005 between 0.25 and 2 kpc, showing that very close to the cold disc (i.e. $h = 0.25$ kpc), there is gas moving due to gravity, rotation and shear. However, due to the lack of SNe, none of this gas is leaving the galaxy.

At the beginning, most of the gas that is pushed to distances $|h| =$ 1 kpc and further away from the galaxy is hot, followed by the warm and cold gas (see Fig. 13). Once the SFR decreases after ~200 Myr, the hot gas, which is mostly the SNe ejecta itself, and the warm gas contribute in similar fractions to the total ouflow rate. Some of the outflowing warm gas also originates from cooled (adiabatically

[10]We used this approach to compare with other simulation results such as Marinacci 2019.

and radiatively) gas that was previously heated by SNe. The vast majority of the inflowing gas is warm, followed by the hot and then cold gas. The ratio of OFR/IFR is higher for the hot than warm gas and smallest for the cold gas. This shows that most of the gas that leaves the galaxy is hot, whereas most of the warm gas falls back even though it reaches as far as 1 kpc away from the galaxy. Only a very small amount of cold gas reaches a distance of 1 kpc away from the galaxy. Similar measurements further away from the galaxy (at $h = \pm 2$ kpc) show that the cold gas does not reach such distances from the galaxy. The cold gas, therefore, contributes little to the total outflow and inflow mass at distances larger than 1 kpc. Mass flow measurements of all the different gas phases closer to the galaxy ($h = \pm(0.25–0.5)$ kpc) show that cold gas gets entrained in the outflows up to these distances. It then, however, quickly falls back onto the galaxy.

The mass flow measurements show that the SNe ejecta are at early times not strong enough to push the gas to large distances and instead immediately fall back onto the galaxy. Later, the SNe push mainly hot ejecta gas far enough from the galaxy such that it does not fall back. The warm and cold gas falls mostly back onto the galaxy, with the warm gas reaching higher distances away from the galaxy. The ejected gas in our simulations is not lost to the galaxy but rather builds a fountain flow where the accreted gas fuels star formation. Such a cycle is important for the metallicity and angular momentum build up of the disc and hot corona (e.g. Marinacci et al. 2010; Übler et al. 2014; Christensen et al. 2016; Anglés-Alcázar et al. 2017). As we will discuss in more detail in the next section, the obtained outflow rates as well as the fountain flow character of the gas in our simulations are comparable to similar galaxy scale simulations.

5 DISCUSSION

In this paper, we present simulations of an MW-like disc galaxy with a turbulent and multiphase ISM structure run with the stellar formation and SNe feedback model of the SATIN project. The goal of this project is to bridge the gap between large and small scales to understand the interaction of AGN feedback with the multiphase gas and how large-scale winds are driven. Because the ISM properties are so tightly linked to star formation and stellar physics we also incorporate a stellar feedback model that regulates star formation as well as the properties of the ISM. For this, we model the formation of star clusters and their individual stellar population with sink particles and follow the evolution of the massive stars formed within the cluster to get realistic SN delay times. The SN implementation in the SATIN model adaptively adjusts to the local environment and switches between the injection of thermal energy and momentum depending on the surroundings. In this paper we discussed in detail the effect of SNe feedback with individual delay time distributions on the multiphase and turbulent ISM as well as compared the results with observations. The inclusion of other stellar feedback processes from massive stars such as radiation and stellar winds is work in progress (Bieri et al. in preparation).

Other simulations in the literature aim to bridge the gap between large-scale models and more detailed ISM simulations for MW-like environments (e.g. Li, Mac Low & Klessen 2005, 2006; Agertz et al. 2013; Rosdahl et al. 2015; Grisdale et al. 2017; Hopkins et al. 2018; Marinacci et al. 2019; Martizzi et al. 2019; Tress et al. 2020) and there is a vast body of work studying the solar neighbourhood ISM and the subsequent outflow properties (see e.g. Kim & Ostriker 2015; Martizzi et al. 2015; Walch et al. 2015; Kim & Ostriker 2018; Moon et al. 2021). In this section, we will discuss the results of the SATIN1 simulations in the context of other full galaxy-scale simulations of MW-like galaxies as well as compare with more detailed ISM studies. Our SATIN model is very similar as used for the stratified solar neighbourhood-like simulations of the SILCC project (Gatto et al. 2017; Peters et al. 2017; Rathjen et al. 2021). Given the comparable setup, this is a great opportunity to compare our results from a full galaxy wide simulation with higher resolution simulations. This will allow us to investigate the need for different stellar feedback channels in light of our results and to determine the need for a more realistic galaxy-scale environment.

We like to emphasize that one novelty of the SATIN model is that it adopts sink particles to model the formation of star clusters as well as that it tracks the evolutionary state of single massive stars to get realistic SNe delay times. The only other full galaxy-scale simulations of MW-like galaxies with a similar sink particle approach are Li et al. (2005, 2006) and Tress et al. (2020). The former present various disc simulations with a gas resolution of $\sim(5–10) \times 10^4$ $M_\odot$ (versus 5×10^3 $M_\odot$ for our simulations) for their two MW-like disc simulations. They also adopted a different star formation model and convert the mass of sink particles into stars using a fixed star formation efficiency. Additionally, they only include stellar feedback implicitly by maintaining a constant gas sound speed. The simulations of Tress et al. (2020) use a very similar sink particle as well as an individual SNe delay time distribution approach (although the exact implementation and treating of the sink particles differ slightly). Because, however, a sink particle approach is not the only possible way of simulating star formation within high-resolution MW-like galaxies we will additionally include in our discussion other simulations of MW-like galaxies using a different approach for star formation and stellar feedback as well as using delay times calculated with the assumption of average stellar populations.

We find that in SATIN1 the interplay between SNe, cooling, gravity, and shear keeps the total SFR within the range of uncertainties of SFR measurements of MW-like galaxy types. In addition, the global SFR surface density moves from the star burst regime above the KS value closer to the KS relation. Interestingly, very similar results have been found by Li et al. (2005, 2006) including stellar feedback only implicitly. Other high-resolution galaxy-scale simulations of MW-like galaxies found that (clustered) SNe exploding in dense environments alone are capable of regulating global star formation as well as producing winds that are highly mass loaded (Martizzi et al. 2019; Tress et al. 2020). Those simulations similarly adopted a more explicit description of ISM physics, star formation, as well as stellar feedback processes. Due to differences in the setup the winds generated in the simulations of Martizzi et al. (2019) have, however, slightly higher mass loading factor ($0.5 \leq \eta \leq 50$) than in our simulations ($1 \leq \eta \leq 10$). Similar to our findings, in their simulations, using only self-gravity and SNe feedback as well, the gas forms cold dense star-forming clouds within which the stars that explode in SNe are born. These dense and cold clouds are generally not disrupted by the SNe (Martizzi et al. 2019; Tress et al. 2020, deduced from Fig. 10 of the latter).

Additionally, we explore in detail the ability of SNe in regulating star formation at different surface densities. To call a region within a galaxy self-regulated we specifically require $\Sigma_{\rm SFR}$, $\Sigma_{\rm gas}$, as well as the VFFs and MFFs to remain constant over a certain time period. We find that SNe manages to regulate star formation at solar neighbourhood surface densities ($r \simeq 7–9$ kpc and $\Sigma_{\rm gas} \sim 10–20$ $M_\odot\,pc^{-2}$) and that it is in these regions self-regulated. This surface density dependent analysis can be compared to detailed simulations that model a portion of the ISM in representative pieces of isolated, stratified, galactic discs with solar neighbourhood-like properties using (magneto-)hydrodynamic (MHD) simulations. Such

simulations have found similar results where SNe feedback alone was strong enough to regulate star formation and the vertical disc structure (Korpi et al. 1999; de Avillez & Breitschwerdt 2004; Joung & Mac Low 2006a; Henley et al. 2015; Girichidis et al. 2016; Kim & Ostriker 2018).

For higher surface density environments, we find that SNe are insufficient in regulating star formation and that gravity and shear are, in our simulations, therefore important drivers of the evolution within these surface densities. Similar conclusions have been found by Moon et al. (2021). They adopt the TIGRESS framework for star formation and SNe feedback for their simulations(Kim & Ostriker 2018)[11] and find that SN feedback is never strong enough to destroy large density environments or quench star formation in high surface density environments. Li et al. (2005, 2006) also report that their results suggest that the non-linear development of gravitational instabilities determine their global and local KS relation. We argue that additional feedback processes, such as ionizing radiation and stellar winds, would be needed in order to further reduce the rate at which stars are formed. Detailed studies of the ISM have shown that ionizing radiation impacts the ambient ISM structure by heating the dense gas phase in star-forming regions, injecting momentum into the ISM and driving local turbulence. This has an effect on gas accretion onto the star clusters and thus further regulates the local efficiency of star formation (Peters, Banerjee & Klessen 2008; Gritschneder et al. 2009; Geen et al. 2015b; Peters et al. 2017; Rathjen et al. 2021). Similar effects have been shown for stellar winds (Gatto et al. 2017), although the relative effect compared to ionizing radiation may, in high-density regions, be lower (Haid et al. 2016; Geen et al. 2021).[12] Promising results from the simulations of (Rathjen et al. 2023) within the SILCC framework show that, for high surface-densities, a feedback model including stellar winds, UV radiation, SNe feedback, as well as CRs together results in the simulations to follow the observed relation between $\Sigma_{\rm gas}$ and $\Sigma_{\rm SFR}$.

Galaxy-scale simulations of MW-like galaxies often try to include such additional feedback processes from massive stars using a sub-grid model approach (Agertz et al. 2013; Hopkins et al. 2018; Marinacci et al. 2019). Their simulations include, on top of a SNe feedback model, many additional stellar feedback channels, such as radiation from stars, stellar winds, as well as photo-electric heating in (Hopkins et al. 2018). They find that the added stellar feedback channels help to regulate and suppress star formation and in some cases help to increase galactic outflows. Interestingly, Agertz et al. (2013) find for their SNe-only simulation a very similar SFR to the one in SATIN1. The sub-grid models used in those simulations rely, however, on a number of assumptions regarding, for instance, the coupling between the radiation and the gas such as the absorption of photons, mean free paths, optical depths, and shielding.

Rosdahl et al. 2015 avoid certain assumptions made in the simulations using a sub-grid model for radiation by tracking the radiation from the stars directly using radiation-hydrodynamics (RHD). They find that for a MW-like galaxy radiation from stars helps to suppress star formation as much as the inclusion of SNe feedback does. This is mainly due to the suppression of dense cloud formation, rather than their destruction due to the radiation. The importance of radiation feedback (mainly photo-heating) to suppress star formation decreases with galaxy mass in their simulations. In future work, it will be interesting to compare our approach following the stellar evolution of individual massive stars and using realistic delay time distributions within the star cluster with the one of Rosdahl et al. (2015) assuming an average stellar population.

We have shown that in SATIN1 SNe launch outflows with mass loading factors comparable with similar high-resolution MW-like simulations such as reported in Martizzi et al. (2019), as well as Marinacci et al. (2019), where they include all their feedback channels.[13] Additionally, looking at the different gas phases in the outflow we have shown that the majority of the gas that leaves the galaxy is hot, whereas the warm and cold gas falls back onto the galaxy. Such a galactic fountain flow that helps to sustain late-time star formation has also been measured in Martizzi et al. (2019) and Marinacci et al. (2019), where most of their ejected gas eventually rains back onto the galactic disc.

At the same time, we do not achieve the strong outflows that are needed in cosmological simulations in order to produce reasonable galaxies in the ΛCDM cosmology (e.g. Muratov et al. 2015; Schaye et al. 2015; Pillepich et al. 2018; Tollet et al. 2019). In addition, the reduction of star formation by a factor of two is insufficient to reproduce the observed stellar mass-to-halo mass relation in cosmological simulations (see e.g. fig. 6 of Hopkins et al. 2014). Future simulations including additional stellar feedback processes will be needed to assess whether such channels help to increase the mass outflows in our simulations. Additionally, cosmological simulations would be helpful to explore the potential of the SATIN model to produce realistic galaxies in a fully cosmological context.[14]

Earlier work by Gatto et al. (2017) and Peters et al. (2017) has shown that a VFF of at least 50 per cent is needed in the hot phase to drive a galactic outflow.[15] This is in line with a measured VFF of around 50 per cent in the hot phase in SATIN1. Following is the VFF of the warm (∼30–35 per cent) and then the cold phase (∼15–20 per cent). These obtained results can be compared to models for the ISM phase VFF that are based on observations of the MW such as those shown in Kalberla & Kerp (2009). Assuming turbulent pressure equilibrium, they derived for the inner 250 pc a VFF in the cold phase of 5–18 per cent, in the warm phase 60–67 per cent (adding the contribution of their warm and warm-hot phase together), and in the hot phase 17–23 per cent (see their fig. 11). Our results for the *SNe* simulation match the VFF of the cold phase, but underestimate/overestimate the VFF in the warm/hot phase. The SNe-only stratified disc simulation by Peters et al. (2017) obtained similar results to our simulations, whereas only their simulation including radiation from the stars approached observed values. This is because radiation disrupts the dense gas in the star-forming regions and increases/decreases the VFF in the warm/hot phase.

The high-density cold gas also makes up ∼80 per cent of the total gas mass in our *SNe* simulation, whereas the analysis by McKee et al. (2015) seems to support that there is a significant fraction (∼50 per cent) of warm gas in the solar neighbourhood. The warm phase also dominates in local shearing box simulations (Kim & Ostriker 2018). On the other hand, the SNe-only stratified disc simulation of Rathjen et al. (2021) get comparable MFFs to our measurements. Only their simulation including radiation and CRs from the stars

[11]The TIGRESS framework uses, along similar lines as adapted here, sink particles to model star formation and SNe feedback.
[12]However, this finding may be also subject to resolution effects.
[13]Note that they report lower SFR as well as lower mass outflow rates leading, however, to a similar mass loading factor.
[14]Given the current implementation such a simulation, while maintaining a good numerical resolution, would be computationally extremely expensive if not impossible.
[15]This assumption has to be modified if cosmic rays are considered in the simulations (see e.g. Peters et al. 2015; Girichidis et al. 2016; Simpson et al. 2016).

reach an MFF of ∼50 per cent. One possible difference between the different simulations might be in the different sink/accretion requirements that, when more strict as in our simulations, might cause more gas to remain cold within a clump rather than being accreted onto a sink. A detailed testing of this hypothesis is beyond the scope of our paper.

By changing the ISM structure, radiation likely also has an effect on the energetics of the ISM. In our simulations, SN feedback alone is not strong enough to disrupt the dense and cold clouds (similar to Rathjen et al. 2021). Looking at the power spectrum of the ISM we find that most of the kinetic power of the cold gas is 'locked-up' in the clumps and that SNe alone are not capable to destroy the dense gas clumps and to drive turbulence in the cold gas on galactic scales. Note, that this might also be additionally enhanced due to the strict sink formation/accretion requirement. In future work we plan to study the effect of radiation on the energetics of the ISM. Along similar lines, adding other early feedback channels such as stellar winds and cosmic ray heating could help to prevent the formation of the coldest gas within the galaxy, and likely have an effect on the energetics of the ISM as well. Getting the VFF and MFF of the different phases correct and including other early feedback processes may also be important for the clustering of SF. Hislop et al. (2022) get, when including only SNe feedback, a clustering that is too high and, similar to our simulation, high-density clumps that are never destroyed.

Finally, we note that we do not only lack early stellar feedback channels, such as radiation and winds, in our simulations but also have not taken into account other important physical processes in our model. Such processes include cosmic ray transport and physics, different cooling and heating processes (such as molecular cooling, cosmic ray and photo-electric heating), magnetic fields, dust production, destruction and evolution (both important for the molecular chemistry as well as for reprocessing radiation fields), and thermal conduction. The inclusion of some of these processes will be part of future work.

In summary, our general results from the SATIN1 simulations are similar to those found in other full MW-like galaxy scale simulations with different implementations of star formation and SNe feedback and similar or coarser resolution. Additionally, the SATIN1 simulations also agree well with detailed stratified-disc simulations that model only portions of the ISM and only include SNe. Our investigation of star formation within different surface densities of the disc and comparing the ISM properties with observations suggests that other feedback channels may be needed in order to better match observed values, especially in higher surface density environments. Detailed ISM simulations have suggested similar in the literature. It will be interesting to investigate this within our SATIN model and additional full galaxy-scale simulations in the future.

6 CONCLUSIONS

In this paper we introduce the star formation and SN feedback model of the SATIN project. The goal of this project is to investigate the interaction between AGN and a turbulent multiphase ISM. We model the formation of star clusters with sink particles and track the evolutionary state of individual massive stars that form within each cluster in order to get realistic SNe delay times. The employed SN model adapts to the local environment depending on whether the cooling radius of the Sedov blast wave is resolved. The SATIN model is a galaxy-wide implementation of a successful ISM model tested in small box simulations and naturally covers an order of magnitude in gas surface density, shear and radial motions. The model is adapted in the AMR code RAMSES. We test the implemented model in high-resolution isolated simulations of an isolated MW-like disc galaxy with a peak resolution of 9 pc. We find that

(i) With SNe feedback the galaxy is globally and within the solar neighbourhood self-regulated and establishes there KS relation that matches within uncertainties with observations.

(ii) Due to SNe feedback, the simulations capture a distinct multiphase ISM with three phases (cold, warm, hot) coexisting and interacting with each other. With SNe, the gas in the ISM covers larger regions in the phase diagram that are thermally unstable. The VFF of the cold phase matches with observations, whereas the VFF of the warm/hot phase are underestimated/overestimated. In addition, we underestimate/overestimate the MFF of the warm/cold gas in the solar neighbourhood.

(iii) SNe are an important driver of the density and energy structure of the ISM. SNe drive additional turbulence in the warm gas and increase the kinetic energy of the cold gas, partly cooling out of the warm phase. A lot of the power of the cold gas is 'locked-up' in the dense cold star forming clouds instead of being disrupted and returned back to the large scale driving. At the same time gravity, shear, and accretion also contribute significantly to the energetic structure of the ISM.

(iv) SN feedback launches outflows with mass loading factors of $3 \leq \eta \leq 10$. The majority of the gas that leaves the galaxy is hot. The warm and cold gas mostly falls back onto the galaxy in a galactic fountain flow.

The inclusion of other stellar feedback processes from massive stars such as radiation and stellar winds seems to be needed in order to reduce the rate at which stars form in higher surface density environments, to increase/decrease the VFF in the warm/hot phase, to prevent the formation of the very cold and dense clouds that we find in the simulations, as well as to increase the MFF of the warm gas. This will be subject of future work (Bieri et. al in preparation).

ACKNOWLEDGEMENTS

We would like to thank the reviewer for carefully reading our paper and for giving such observant, detailed, and constructive comments that substantially improved the quality of this paper. We thank Freeke van de Voort and Francesca Fragkoudi for helpful comments on the manuscript as well as interesting discussions. RB acknowledges support from The Exoclimes Simulation Platform: General Tools for Understanding Exoplanet Atmospheres. TN acknowledges support from the Deutsche Forschungsgemeinschaft (DFG, German Research Foundation) under Germany's Excellence Strategy – EXC-2094 – 390783311 from the DFG Cluster of Excellence 'ORIGINS'. SG acknowledges support from a NOVA grant for the theory of massive star formation. During the time of her main contribution to this work, RB has been employed by the Max-Planck-Institute for Astrophysics in Garching and JPC was employed at the Technical University of Munich.

DATA AVAILABILITY

The simulation data used within this paper will be shared on reasonable request to the corresponding author.

REFERENCES

Abadi M. G., Navarro J. F., Steinmetz M., Eke V. R., 2003, ApJ, 591, 499
Agertz O., Kravtsov A. V., Leitner S. N., Gnedin N. Y., 2013, ApJ, 770, 25

Agertz O., Romeo A. B., Grisdale K., 2015, MNRAS, 449, 2156
Andersson E. P., Agertz O., Renaud F., 2020, MNRAS, 494, 3328
Andersson E. P., Renaud F., Agertz O., 2021, MNRAS, 502, L29
Anglés-Alcázar D., Faucher-Giguère C.-A., Kereš D., Hopkins P. F., Quataert E., Murray N., 2017, MNRAS, 470, 4698
Antonuccio-Delogu V., Silk J., 2010, MNRAS, 405, 1303
Balbus S. A., Hawley J. F., 1991, ApJ, 376, 214
Benson A. J., Bower R. G., Frenk C. S., Lacey C. G., Baugh C. M., Cole S., 2003, ApJ, 599, 38
Bicknell G. V., Sutherland R. S., van Breugel W. J. M., Dopita M. A., Dey A., Miley G. K., 2000, ApJ, 540, 678
Bieri R., Dubois Y., Rosdahl J., Wagner A., Silk J., Mamon G. A., 2017, MNRAS, 464, 1854
Binney J., 1977, ApJ, 215, 483
Black J. H., 1981, MNRAS, 197, 553
Bleuler A., Teyssier R., 2014, MNRAS, 445, 4015
Blondin J. M., Wright E. B., Borkowski K. J., Reynolds S. P., 1998, ApJ, 500, 342
Booth C. M., Schaye J., 2009, MNRAS, 398, 53
Bournaud F., Elmegreen B. G., Teyssier R., Block D. L., Puerari I., 2010, MNRAS, 409, 1088
Burgers J., 1948, Von Mises Richard, Von Kármán Theodore, A Mathematical Model Illustrating the Theory of Turbulence, Elsevier, p. 1, 171, https://www.sciencedirect.com/science/article/pii/S0065215608701005
Cen R., 1992, ApJS, 78, 341
Cen R., Ostriker J. P., 1992, ApJ, 399, L113
Chevalier R. A., 1974, ApJ, 188, 501
Christensen C. R., Davé R., Governato F., Pontzen A., Brooks A., Munshi F., Quinn T., Wadsley J., 2016, ApJ, 824, 57
Combes F. et al., 2012, A&A, 539, A67
Courant R., Friedrichs K., Lewy H., 1928, Math. Ann., 100, 32
Cox D. P., Smith B. W., 1974, ApJ, 189, L105
Creasey P., Theuns T., Bower R. G., Lacey C. G., 2011, MNRAS, 415, 3706
Dale J. E., Ngoumou J., Ercolano B., Bonnell I. A., 2014, MNRAS, 442, 694
de Avillez M. A., Breitschwerdt D., 2004, A&A, 425, 899
Dekel A., Silk J., 1986, ApJ, 303, 39
Di Matteo T., Springel V., Hernquist L., 2005, Nature, 433, 604
Di Matteo T., Colberg J., Springel V., Hernquist L., Sijacki D., 2008, ApJ, 676, 33
Díaz-Rodríguez M., Murphy J. W., Rubin D. A., Dolphin A. E., Williams B. F., Dalcanton J. J., 2018, ApJ, 861, 92
Dorfi E. A., Breitschwerdt D., 2012, A&A, 540, A77
Dubois Y., Teyssier R., 2008, in Knapen J. H., Mahoney T. J., Vazdekis A., eds, ASP Conf. Ser. Vol. 390, Pathways Through an Eclectic Universe. Astron. Soc. Pac., San Francisco, p. 388
Dubois Y., Devriendt J., Slyz A., Teyssier R., 2012, MNRAS, 420, 2662
Dubois Y. et al., 2014, MNRAS, 444, 1453
Dutta P., Bharadwaj S., 2013, MNRAS, 436, L49
Dutta P., Begum A., Bharadwaj S., Chengalur J. N., 2009a, MNRAS, 398, 887
Dutta P., Begum A., Bharadwaj S., Chengalur J. N., 2009b, in Saikia D. J., Green D. A., Gupta Y., Venturi T., eds, ASP Conf. Ser. Vol. 407, The Low-Frequency Radio Universe. Astron. Soc. Pac., San Francisco, p. 83,
Díaz-Rodríguez M., Murphy J. W., Williams B. F., Dalcanton J. J., Dolphin A. E., 2021, MNRAS, 506, 781
Efstathiou G., 2000, MNRAS, 317, 697
Ekström S. et al., 2012, A&A, 537, A146
Elmegreen B. G., Scalo J., 2004, ARA&A, 42, 211
Elmegreen B. G., Kim S., Staveley-Smith L., 2001, ApJ, 548, 749
Emerick A., Bryan G. L., Mac Low M.-M., 2019, MNRAS, 482, 1304
Faucher-Giguère C.-A., Lidz A., Zaldarriaga M., Hernquist L., 2009, ApJ, 703, 1416
Federrath C., Klessen R. S., 2012, ApJ, 761, 156
Federrath C., Klessen R. S., Schmidt W., 2009, ApJ, 692, 364
Federrath C., Banerjee R., Clark P. C., Klessen R. S., 2010, ApJ, 713, 269
Ferland G. J., Korista K. T., Verner D. A., Ferguson J. W., Kingdon J. B., Verner E. M., 1998, PASP, 110, 761
Ferrière K. M., 2001, Rev. Mod. Phys., 73, 1031
Gaibler V., Khochfar S., Krause M., Silk J., 2012, MNRAS, 425, 438
Gammie C. F., Ostriker J. P., Jog C. J., 1991, ApJ, 378, 565
Gatto A. et al., 2015, MNRAS, 449, 1057
Gatto A. et al., 2017, MNRAS, 466, 1903
Geen S., Rosdahl J., Blaizot J., Devriendt J., Slyz A., 2015a, MNRAS, 448, 3248
Geen S., Hennebelle P., Tremblin P., Rosdahl J., 2015b, MNRAS, 454, 4484
Geen S., Watson S. K., Rosdahl J., Bieri R., Klessen R. S., Hennebelle P., 2018, MNRAS, 481, 2548
Geen S., Bieri R., Rosdahl J., de Koter A., 2021, MNRAS, 501, 1352
Girichidis P. et al., 2016, MNRAS, 456, 3432
Girichidis P., Naab T., Hanasz M., Walch S., 2018, MNRAS, 479, 3042
González Delgado R. M. et al., 2017, A&A, 607, A128
Grisdale K., Agertz O., Romeo A. B., Renaud F., Read J. I., 2017, MNRAS, 466, 1093
Gritschneder M., Naab T., Walch S., Burkert A., Heitsch F., 2009, ApJ, 694, L26
Grudić M. Y., Guszejnov D., Offner S. S. R., Rosen A. L., Raju A. N., Faucher-Giguère C.-A., Hopkins P. F., 2022, MNRAS, 512, 216
Guillet T., Teyssier R., 2011, J. Comput. Phys., 230, 4756
Guszejnov D., Grudić M. Y., Hopkins P. F., Offner S. S. R., Faucher-Giguère C.-A., 2021, MNRAS, 502, 3646
Guszejnov D., Grudić M. Y., Offner S. S. R., Faucher-Giguère C.-A., Hopkins P. F., Rosen A. L., Effects of the environment and feedback physics on the initial mass function of stars in the STARFORGE simulations, MNRAS, 515, 2022, 4929, doi:10.1093/mnras/stac2060
Gutcke T. A., Pakmor R., Naab T., Springel V., 2022, MNRAS, 513, 1372
Haardt F., Madau P., 1996, ApJ, 461, 20
Haid S., Walch S., Naab T., Seifried D., Mackey J., Gatto A., 2016, MNRAS, 460, 2962
Haid S., Walch S., Seifried D., Wünsch R., Dinnbier F., Naab T., 2018, MNRAS, 478, 4799
Haiman Z., Rees M. J., Loeb A., 1996, ApJ, 467, 522
Hanasz M., Strong A. W., Girichidis P., 2021, Liv. Rev. Comput. Astrophys., 7, 2
Henley D. B., Shelton R. L., Kwak K., Hill A. S., Mac Low M.-M., 2015, ApJ, 800, 102
Hernquist L., 1990, ApJ, 356, 359
Hislop J. M., Naab T., Steinwandel U. P., Lahén N., Irodotou D., Johansson P. H., Walch S., 2022, MNRAS, 509, 5938
Hoffmann V., Romeo A. B., 2012, MNRAS, 425, 1511
Hopkins P. F., Kereš D., Oñorbe J., Faucher-Giguère C.-A., Quataert E., Murray N., Bullock J. S., 2014, MNRAS, 445, 581
Hopkins P. F. et al., 2018, MNRAS, 480, 800
Hu J., 2008, MNRAS, 386, 2242
Hu C.-Y., Naab T., Walch S., Glover S. C. O., Clark P. C., 2016, MNRAS, 458, 3528
Hu C.-Y., Naab T., Glover S. C. O., Walch S., Clark P. C., 2017, MNRAS, 471, 2151
Hui L., Gnedin N. Y., 1997, MNRAS, 292, 27
Hummels C. B., Bryan G. L., 2012, ApJ, 749, 140
Iffrig O., Hennebelle P., 2015, A&A, 576, A95
Joung M. K. R., Mac Low M.-M., 2006a, ApJ, 653, 1266
Joung M. K. R., Mac Low M.-M., 2006b, ApJ, 653, 1266
Kalberla P. M. W., Kerp J., 2009, ARA&A, 47, 27
Kannan R., Vogelsberger M., Stinson G. S., Hennawi J. F., Marinacci F., Springel V., Macciò A. V., 2016, MNRAS, 458, 2516
Katz N., 1992, ApJ, 391, 502
Kennicutt R. C., Jr, 1998b, ApJ, 498, 541
Kennicutt R. C., Jr, 1998a, ApJ, 498, 541
Kennicutt R. C., Evans N. J., 2012, ARA&A, 50, 531
Kim C.-G., Ostriker E. C., 2015, ApJ, 802, 99
Kim C.-G., Ostriker E. C., 2018, ApJ, 853, 173
Kim C.-G., Ostriker E. C., Kim W.-T., 2013, ApJ, 776, 1
Kim J.-G., Kim W.-T., Ostriker E. C., 2019, ApJ, 883, 102
Kimm T., Cen R., 2014, ApJ, 788, 121
Kimm T., Cen R., Devriendt J., Dubois Y., Slyz A., 2015, MNRAS, 451, 2900

Kimm T., Haehnelt M., Blaizot J., Katz H., Michel-Dansac L., Garel T., Rosdahl J., Teyssier R., 2018, MNRAS, 475, 4617
Klessen R. S., Glover S. C. O., 2016, Saas-Fee Advanced Course, 43, 85
Kolmogorov A. N., 1991, Proc. R. Soc. Lond. Ser. A, 434, 9
Kormendy J., Ho L. C., 2013, ARA&A, 51, 511
Kormendy J., Bender R., Cornell M. E., 2011, Nature, 469, 374
Korpi M. J., Brandenburg A., Shukurov A., Tuominen I., Nordlund Å., 1999, ApJ, 514, L99
Kowal G., Lazarian A., 2007, ApJ, 666, L69
Kritsuk A. G., Norman M. L., Padoan P., Wagner R., 2007, ApJ, 665, 416
Krumholz M. R., Burkhart B., 2016, MNRAS, 458, 1671
Lahén N., Naab T., Johansson P. H., Elmegreen B., Hu C.-Y., Walch S., Steinwandel U. P., Moster B. P., 2020, ApJ, 891, 2
Lancaster L., Ostriker E. C., Kim J.-G., Kim C.-G., 2021, ApJ, 922, L3
Leitherer C. et al., 1999, ApJS, 123, 3
Leroy A. K., Walter F., Brinks E., Bigiel F., de Blok W. J. G., Madore B., Thornley M. D., 2008, AJ, 136, 2782
McKee C. F., Ostriker E. C., 2007, ARA&A, 45, 565
Li Y., Mac Low M.-M., Klessen R. S., 2005, ApJ, 626, 823
Li Y., Mac Low M.-M., Klessen R. S., 2006, ApJ, 639, 879
Li M., Bryan G. L., Ostriker J. P., 2017, ApJ, 841, 101
Lodders K., Palme H., Gail H. P., 2009, Solar System, Landolt-Börnstein - Group VI Astronomy and Astrophysics. Springer-Verlag, Berlin and Heidelberg
McKee C. F., Ostriker J. P., 1977, ApJ, 218, 148
McKee C. F., Parravano A., Hollenbach D. J., 2015, ApJ, 814, 13
Mac Low M.-M., Klessen R. S., 2004, Rev. Mod. Phys., 76, 125
Mackey J., Gvaramadze V. V., Mohamed S., Langer N., 2015, A&A, 573, A10
Magorrian J. et al., 1998, AJ, 115, 2285
Marinacci F., Binney J., Fraternali F., Nipoti C., Ciotti L., Londrillo P., 2010, MNRAS, 404, 1464
Marinacci F., Pakmor R., Springel V., 2014, MNRAS, 437, 1750
Marinacci F., Sales L. V., Vogelsberger M., Torrey P., Springel V., 2019, MNRAS, 489, 4233
Martizzi D., Faucher-Giguère C.-A., Quataert E., 2015, MNRAS, 450, 504
Martizzi D., Fielding D., Faucher-Giguère C.-A., Quataert E., 2016, MNRAS, 459, 2311
Martizzi D., Quataert E., Faucher-Giguère C.-A., Fielding D., 2019, MNRAS, 483, 2465
Meidt S. E. et al., 2018, ApJ, 854, 100
Moon S., Kim W.-T., Kim C.-G., Ostriker E. C., 2021, ApJ, 914, 9
Murante G., Monaco P., Borgani S., Tornatore L., Dolag K., Goz D., 2015, MNRAS, 447, 178
Muratov A. L., Kereš D., Faucher-Giguère C.-A., Hopkins P. F., Quataert E., Murray N., 2015, MNRAS, 454, 2691
Naab T., Ostriker J. P., 2017, ARA&A, 55, 59
Nakamura F., Li Z.-Y., 2007, ApJ, 662, 395
Navarro J. F., White S. D. M., 1993, MNRAS, 265, 271
Navarro J. F., Frenk C. S., White S. D. M., 1996, ApJ, 462, 563
Nusser A., Silk J., 2022, MNRAS, 509, 2979
Osterbrock D. E., Ferland G. J., University Science Books, Sausalito, CA, 2006, Astrophysics of Gaseous Nebulae and Active Galactic Nuclei.
Ostriker E. C., Shetty R., 2011, ApJ, 731, 41
Padoan P., Kim S., Goodman A., Staveley-Smith L., 2001, ApJ, 555, L33
Padoan P., Federrath C., Chabrier G., Evans N. J. II, Johnstone D., Jørgensen J. K., McKee C. F., Nordlund Å., The Star Formation Rate of Molecular Clouds 2014, in Beuther H., Klessen R. S., Dullemond C. P., Henning T., eds, Protostars and Planets VI. p. 77
Padoan P., Pan L., Haugbølle T., Nordlund Å., 2016, ApJ, 822, 11
Perret V., 2016, Astrophysics Source Code Library, record ascl:1607.002
Peters T., Banerjee R., Klessen R. S., 2008, Phys. Scr. Vol. T, 132, 014026
Peters T. et al., 2015, ApJ, 813, L27
Peters T. et al., 2017, MNRAS, 466, 3293
Pfrommer C., Werhahn M., Pakmor R., Girichidis P., Simpson C. M., 2022, MNRAS, 515, 4229
Pillepich A. et al., 2018, MNRAS, 473, 4077
Piontek R. A., Ostriker E. C., 2004, ApJ, 601, 905
Rathjen T.-E. et al., 2021, MNRAS, 504, 1039
Rathjen T.-E., Naab T., Walch S., Seifried D., Girichidis P., Wünsch R., 2023, MNRAS, 522, 1843
Rees M. J., Ostriker J. P., 1977, MNRAS, 179, 541
Renaud F., Kraljic K., Bournaud F., 2012, ApJ, 760, L16
Rey M. P., Pontzen A., Agertz O., Orkney M. D. A., Read J. I., Rosdahl J., 2020, MNRAS, 497, 1508
Romeo A. B., Agertz O., 2014, MNRAS, 442, 1230
Romeo A. B., Burkert A., Agertz O., 2010, MNRAS, 407, 1223
Rosdahl J., Blaizot J., Aubert D., Stranex T., Teyssier R., 2013, MNRAS, 436, 2188
Rosdahl J., Schaye J., Teyssier R., Agertz O., 2015, MNRAS, 451, 34
Rosen A., Bregman J. N., 1995, ApJ, 440, 634
Saintonge A., Catinella B., 2022, ARA\&A, 60, 319, preprint (arXiv:2202.00690)
Sales L. V., Navarro J. F., Schaye J., Dalla Vecchia C., Springel V., Booth C. M., 2010, MNRAS, 409, 1541
Salpeter E. E., 1955, ApJ, 121, 161
Schaye J. et al., 2015, MNRAS, 446, 521
Schmidt M., 1959, ApJ, 129, 243
Schmidt W., Federrath C., Klessen R., 2008, Phys. Rev. Lett., 101, 194505
Sijacki D., Springel V., Di Matteo T., Hernquist L., 2007, MNRAS, 380, 877
Silk J., 1977, ApJ, 211, 638
Silk J., Rees M. J., 1998, A&A, 331, L1
Simpson C. M., Pakmor R., Marinacci F., Pfrommer C., Springel V., Glover S. C. O., Clark P. C., Smith R. J., 2016, ApJ, 827, L29
Slyz A. D., Devriendt J. E. G., Bryan G., Silk J., 2005, MNRAS, 356, 737
Smith M. C., Bryan G. L., Somerville R. S., Hu C.-Y., Teyssier R., Burkhart B., Hernquist L., 2021, MNRAS, 506, 3882
Somerville R. S., Davé R., 2015, ARA&A, 53, 51
Stanimirovic S., Staveley-Smith L., Dickey J. M., Sault R. J., Snowden S. L., 1999, MNRAS, 302, 417
Steinwandel U. P., Bryan G. L., Somerville R. S., Hayward C. C., Burkhart B., 2022, preprint (arXiv:2205.09774)
Stinson G., Seth A., Katz N., Wadsley J., Governato F., Quinn T., 2006, MNRAS, 373, 1074
Sutherland R. S., Bicknell G. V., 2007, ApJS, 173, 37
Teyssier R., 2002, A&A, 385, 337
Thornton K., Gaudlitz M., Janka H. T., Steinmetz M., 1998, ApJ, 500, 95
Tollet É., Cattaneo A., Macciò A. V., Dutton A. A., Kang X., 2019, MNRAS, 485, 2511
Toro E. F., Spruce M., Speares W., 1994, Shock Waves, 4, 25
Tress R. G., Smith R. J., Sormani M. C., Glover S. C. O., Klessen R. S., Mac Low M.-M., Clark P. C., 2020, MNRAS, 492, 2973
Truelove J. K., Klein R. I., McKee C. F., Holliman J. H. II], Howell L. H., Greenough J. A., 1997, ApJ, 489, L179
Übler H., Naab T., Oser L., Aumer M., Sales L. V., White S. D. M., 2014, MNRAS, 443, 2092
Verliat A., Hennebelle P., González M., Lee Y.-N., Geen S., A&A, 2022, 663
Vogelsberger M. et al., 2014, MNRAS, 444, 1518
Wada K., 2008, ApJ, 675, 188
Wada K., Meurer G., Norman C. A., 2002, ApJ, 577, 197
Wagner A. Y., Bicknell G. V., 2011, ApJ, 728, 29
Walch S., Naab T., 2015, MNRAS, 451, 2757
Walch S. K., Whitworth A. P., Bisbas T., Wünsch R., Hubber D., 2012, MNRAS, 427, 625
Walch S. et al., 2015, MNRAS, 454, 238
Wang P., Li Z.-Y., Abel T., Nakamura F., 2010, ApJ, 709, 27
Wang L., Dutton A. A., Stinson G. S., Macciò A. V., Penzo C., Kang X., Keller B. W., Wadsley J., 2015, MNRAS, 454, 83
White S. D. M., Rees M. J., 1978, MNRAS, 183, 341
Zhang H.-X., Hunter D. A., Elmegreen B. G., 2012, ApJ, 754, 29
Zhou S., Aragón-Salamanca A., Merrifield M., Andrews B. H., Drory N., Lane R. R., 2023, MNRAS, 521, 5810

APPENDIX A: TEST SIMULATIONS OF SN MODEL

To test the SN feedback scheme, we performed idealised simulations and placed a single SN in a uniform density ($n_{\rm H}$ = 10 H cm^{-3}) medium with solar metallicity. The radiative cooling described above is included in all simulations. Note that we follow a very similar approach as the test simulations performed in Kimm & Cen (2014).

To test whether the implemented feedback model preserves the radial momentum independent of the resolution employed, we performed five simulations with varying resolution changing from 1 to 16 pc. Fig. A1 shows the radial momentum from the explosion at the momentum-conserving phase at t = 0.1 Myr (see Blondin et al. 1998; Thornton et al. 1998). The dashed grey line shows the radial momentum in the shell predicted from equation (5) and the red vertical line shows the radius of the bubble at the end of the Sedov–Taylor phase $R_{\rm ST}$ = 7.4 pc; (see equation 2 and Blondin et al. 1998). The red circles and green triangles show the momentum transfer from the explosion to the surrounding gas using the thermal and momentum input scheme, respectively. As Kimm & Cen (2014) already noted, the mass swept up by the SN ejecta differs between resolution. Therefore the different resolution runs correspond in practice to different stages of the explosion from the adiabatic to momentum-conserving phase. In our SN feedback model, we switch to a momentum-input scheme in the case of an unresolved Sedov–Taylor phase. In practice, we inject momentum rather than thermal energy if $R_{\rm ST} < R_{\rm inj} = 3 \times \Delta x$. This corresponds in our test simulation setup to a switch to a momentum-input with a resolution of $\Delta x \geq 2.6$ pc. With this, we ensure that, if we inject thermal energy, the local cooling radius is sufficiently resolved by at least three resolution elements along each Cartesian axis. Fig. A1 shows that the feedback scheme transfers approximately the same of momentum. The measured total momentum is roughly 5 per cent smaller than the prediction by 1D hydrodynamics simulations (Thornton et al. 1998).[16] The results from the thermal to the mechanical input model are very similar for high resolution simulations ($\Delta x \lesssim 3$ pc). As is already well known (Katz 1992; Navarro & White 1993; Abadi et al. 2003; Slyz et al. 2005; Stinson et al. 2006; Creasey et al. 2011; Hummels & Bryan 2012; Kimm & Cen 2014), the thermal feedback scheme exhibits the overcooling problem in lower resolution runs where the cooling radius is underresolved ($\Delta x \gtrsim 3$ pc).

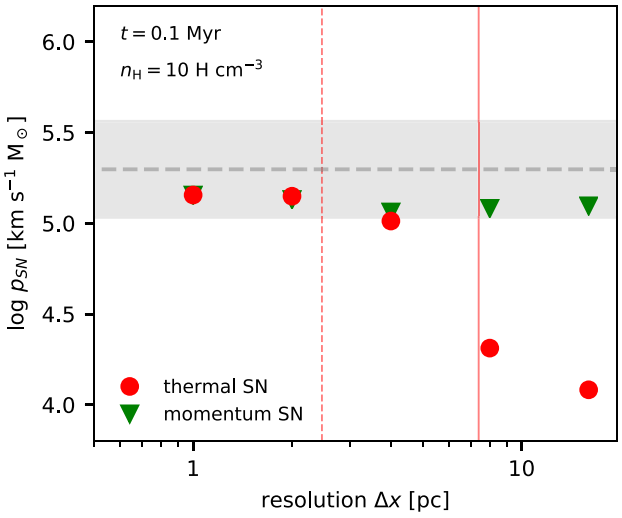

Figure A1. Momentum transfer from a single SN in a uniform density of $n_{\rm H}$ = 10 H cm^{-3}, solar metallicity, and radiative cooling enabled. We performed five simulations and varied the resolution from 1 to 16 pc. We measured the momentum at the momentum-conserving phase of the Sedov solution (0.1 Myr). The measurements can be compared to the prediction of one dimensional models given in equation (5) (see also Blondin et al. 1998; Thornton et al. 1998). The red circles and green triangles show the momentum transfer from the explosion to the surrounding gas using the thermal and momentum input scheme, respectively. The red vertical line shows the radius of the bubble at the end of the Sedov–Taylor phase at $R_{\rm ST}$ = 7.4 pc??? (see equation 2 and Blondin et al. 1998). In the test simulation conditions, the switch between the thermal-input and momentum-input scheme would be at Δx = 2.6 pc (red dotted line). This shows that with our SN feedback scheme, we transfer roughly the same amount of momentum at the snow-plow phase independent of the resolution employed.

APPENDIX B: EFFECT OF RESOLUTION ON STAR FORMATION

In order to test the effect of resolution on the formation of stars in our galaxy we have performed two other simulations, including SNe feedback, with progressively lower resolution: 18 (=2 × standard resolution) and 36 pc (=4 × standard resolution). In addition to the lower cell resolution, we also changed the refinement criteria where in the lower resolution simulations a cell is refined if the gas within a cell is larger than 5 × 10^4 and 5 × 10^5 M$_\odot$, respectively, instead of 5 × 10^3 M$_\odot$ as for the standard resolution. Everything else is kept the same between the different simulations (i.e. initial condition, number of stellar and DM particles, sink formation threshold) in order to best test the effect of gas resolution on the SFR within the galaxy. Fig. B1 shows in the left-hand panel the global observed SFR history for the different resolution simulations (including the default simulation *SNe*) as well as the *nSNe* simulation. The different resolution simulations agree quite well with each other. This is again confirmed in the right-hand panel showing the total integrated stellar mass formed. Here the value for all the SNe simulations at different resolutions converge towards a similar value. The decrease in SFR for all the simulations is more stochastic when SNe is included and stronger with lower resolution. This could be because in lower resolution simulations the SNe manage to disrupt or destroy the high-density gas more effectively causing the SFR to drop momentarily, only to increase when gas starts to collapse towards the high-density clouds and stars start to form again. This also causes the total amount of formed stars to be slightly lower the coarser the resolution. Such complexities indicate that convergence (in this context convergence of star formation and the properties of the ISM within the galaxy) continues to pose a challenge for galaxy formation models.

[16] Kimm & Cen reported a 20 per cent difference with their scheme.

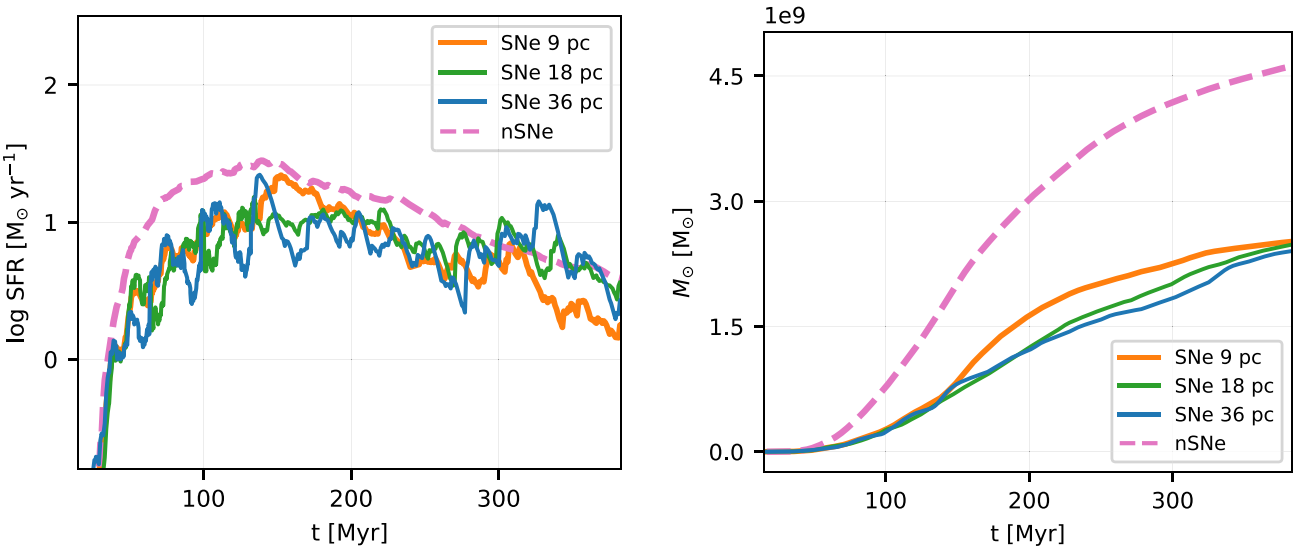

Figure B1. Left-hand panel: global observed SFR history (see equation 9) for SNe simulations with different resolution (9 pc as standard, 18 pc, and 36 pc) in comparison with the *nSNe* simulation. The dashed pink and orange line are the same as in Fig. 5. The global SFR of the lower resolution simulations agree, especially at the beginning, quite well with the default *SNe* simulation. When including SNe feedback the SFR oscillates more, the coarser the resolution. The SFR of the *nSNe* simulation is noticeably smoother than the SNe simulations. After an initial rise, the SFR decrease for all the simulations but much more stochastically when SNe is included. Towards the end of the simulations resolution has a comparable relative effect on the SFR as the SNe explosions. Right-hand panel: the fact that the different resolutions agree well with each other is also clear from the total integrated stellar mass formed. All the different resolution simulations converge towards a similar value. The *nSNe* simulation transforms much more gas into stars, as already discussed in the main text above (see Section 4.2).

APPENDIX C: COMPUTING POWER SPECTRA

We quantify the kinetic state of the ISM in Fourier space by first calculating the kinetic energy power spectra and then divide it by the mass within the box to get the specific kinetic energy power spectra (see Section 4.3). This improves the comparison between simulations. The kinetic energy power spectra of the weight w is defined as

$$P(\boldsymbol{k}) = \tilde{w}(\boldsymbol{k}) \cdot w(\boldsymbol{k})^*, \tag{C1}$$

where $\tilde{w}(\boldsymbol{k})$ is the Fourier transform of the real array $w(\boldsymbol{k})$, $\boldsymbol{k}$ is the wave vector, and '$*$' refers to the complex-conjugate. To get the Fourier transform of the kinetic energy field, we used $w = \sqrt{\rho}\boldsymbol{v}(\boldsymbol{r})$. Here $\boldsymbol{v}(\boldsymbol{r})$ is the three-dimensional velocity vector at cell centre $\boldsymbol{r}$ (measured in our case from the centre of the galaxy) and ρ the total density within each simulation cell. With this choice of weights, the power spectrum directly measures the kinetic energy (see also Grisdale et al. 2017). Another weight that is often used ($w = \rho^{1/3}\boldsymbol{v}$) corresponds to a kinetic energy flux and has been shown to reproduce energy spectra with Kolmogorov scaling ($e_k \propto \boldsymbol{k}^{-5/3}$) in super-sonic flows see Kowal & Lazarian 2007; Kritsuk et al. 2007; Schmidt, Federrath & Klessen 2008; Federrath, Klessen & Schmidt 2009, for this choice.

We calculate the power spectrum within an $\sim 10 \times 10 \times 10$ kpc^3 region centred on the galaxy.[17] For all of the spectra we use a uniform grid of resolution $\sim$40 pc and account for the non-periodic boundary by zero-padding the calculated cubes. The length of the void domain is in each dimension set to be twice as big as the chosen box size. We experimented with more padding as well as different box sizes and confirmed that the main results and findings are not altered.

To obtain the power spectrum $P(\boldsymbol{k})$ of the specific kinetic energy, we first Fourier transform the cube, bin $P(\boldsymbol{k})$ in wave vectors $k = |\boldsymbol{k}|$, normalize by the area of the spherical surface with radius $k + 0.5$, and finally divide it by the total mass within the box. This finally gives the 'angle-averaged' specific kinetic energy spectrum (e.g. Joung & Mac Low 2006b), $\langle P(k) \rangle$, where the physical scale l is connected to the wave vector via $k = 2\pi/l$.

[17] More precisely, we calculate the size of the box for the power spectrum such that a power of two number of cells covers the region using the given cell resolution.

This paper has been typeset from a TEX/LATEX file prepared by the author.